# Enhanced Bonding of Pentagon-Heptagon Defects in Graphene to Metal Surfaces: Insights from the Adsorption of Azulene and Naphthalene to Pt(111)

Benedikt P. Klein<sup>a</sup>, S. Elizabeth Harman<sup>b</sup>, Lukas Ruppenthal<sup>a</sup>, Griffin M. Ruehl<sup>b</sup>, Samuel J. Hall<sup>c,d</sup>, Spencer J. Carey<sup>b</sup>, Jan Herritsch<sup>a</sup>, Martin Schmid<sup>a</sup>, Reinhard J. Maurer<sup>d</sup>, Ralf Tonner<sup>a</sup>, Charles T. Campbell<sup>b</sup>, J. Michael Gottfried<sup>a</sup>

<sup>a</sup>Fachbereich Chemie, Philipps-Universität Marburg, Hans-Meerwein-Straße. 4, 35032 Marburg, Germany

<sup>b</sup>Department of Chemistry, University of Washington, Bagley Hall, Seattle, WA 98195, United States of America

<sup>c</sup>MAS Centre for Doctoral Training, Senate House, and <sup>d</sup>Department of Chemistry and Centre for Scientific Computing, University of Warwick, Gibbet Hill Road, Coventry, CV4 7AL, United Kingdom

#### **ABSTRACT**

The performance of graphene-based (opto)electronic devices depends critically on the graphene/metal interface formed at the metal contacts. We show here that the interface properties may be controlled by topological defects, such as the pentagon-heptagon (5-7) pairs, because of their strongly enhanced bonding to the metal. To measure the bond energy and other key properties not accessible for the embedded defects, we use azulene as a molecular model for the 5-7 defect. Comparison to its isomer naphthalene, which represents the regular graphene structure, reveals that azulene interacts more strongly with a Pt(111) surface. Its adsorption energy, as measured by single-crystal adsorption calorimetry (SCAC), exceeds that of naphthalene by up to 116 kJ/mol (or up to 50%). Both isomers undergo hybridization of their frontier orbitals with metal states, as indicated by photoelectron (XPS/UPS) and near-edge X-ray absorption fine structure (NEXAFS) spectroscopy combined with MO-projection analysis through dispersion corrected, periodic density functional theory (DFT) calculations. Based on the NEXAFS/DFT analysis, the stronger bond of the 5-7 system is attributed to the different energetic response of its unoccupied frontier orbitals to adsorption. Adsorption-induced bond-length changes show substantial topology-related differences between the isomers. Electron transfer occurs in both directions through donation/back-donation, resulting in the partial occupation (deoccupation) of formerly unoccupied (occupied) orbitals, as revealed by energy decomposition analysis for extended systems (pEDA). Our model study shows that the topology of the  $\pi$ -electron system strongly affects its bonding to a transition metal and thus can be utilized to tailor interface properties.

## **INTRODUCTION**

Graphene as one of the most prominent two-dimensional (2D) materials is known for the exceptional electronic and mechanical properties of its ideal lattice. Large-scale graphene samples, however, are always polycrystalline and contain topological defects, such as pentagons, heptagons and pentagon-heptagon (5-7) pairs (Figure 1a), especially at grain boundaries. These defects, which are induced by rearrangement of carbon-carbon (C-C) bonds, strongly influence the chemical and physical properties of graphene, including chemical reactivity, he mechanical strength, electron transport, and magnetism. Their utilization for tailoring the properties of graphene through topological design has been proposed.

Interfaces between graphene and metals are formed during the epitaxial growth of the 2D material on metallic substrates. 15 They also play a prominent role in graphene-based electronic devices, where metal contacts are necessary. 16 The properties of the resulting graphene/metal interfaces control important performance-determining parameters such as the contact resistance. 17 Considering the substantial influences of defects on the properties of graphene, it is likely that they also affect the interfacial interaction, as indicated by the reduced resistances observed for contacts to graphene edges. 16 However, the bonding of intrinsic graphene defects to metals is largely unexplored, mainly due to the experimental challenges arising from the investigations of embedded defects in low concentrations. Expanding on a recently introduced approach, 18 we use here a molecular model system to study the bonding of 5-7 graphene defects to the reactive Pt(111) surface. In this model, azulene with its 5-7 ring structure represents the defect, whereas its isomer naphthalene is the reference molecule representing the hexagonal rings of defect-free graphene (Figure 1b,c). The 5-7 motif was chosen because it is the most abundant building block for topological defects. It occurs in isolated 5-7 defects, in pairs as Stone-Wales defects, or in chains at grain boundaries. In addition, the 5-7 motif represents a class of defects for which a molecular model can be contrived, unlike vacancies. The model system approach allows for the application of laterally integrating techniques and thus provides unique access to parameters that cannot be measured for the real embedded defects, such as bond energies. Even though naphthalene is strongly chemisorbed on Pt(111), <sup>19</sup> we find here that azulene binds even stronger with adsorption energies that are up to 50% higher.

To concisely describe the topological properties of the defect, we use here the established concept of alternant versus non-alternant topology.<sup>20</sup> In the alternant conjugated system of naphthalene (and regular graphene), the carbon atoms can be labeled in an alternating fashion (*e.g.* red and green as in Figure 1b,c), while this is not possible for a non-alternant system like azulene (or the 5-7 defect). The non-alternant topology leads to the violation of the Coulson-Rushbrooke pairing theorem and thus to a distinctly different valence electronic structure.<sup>21</sup> In our model molecules, this electronic difference is manifested in the large dipole moment (0.8 D)<sup>22</sup> and intense blue color of azulene, whereas naphthalene has no dipole moment and is colorless.

The importance of non-alternant aromatic structures extends far beyond their role as graphene defects. Recently, they have found attention for application as molecular or polymeric organic semiconductors in organic (opto)electronic devices, because of their low band gaps and high charge carrier mobilities.<sup>23</sup> Their interfaces to metal electrodes, which are known to strongly influence the properties of the device,<sup>24-25</sup> have only rarely been studied, unlike interfaces to alternant aromatic systems.<sup>26</sup> Comparative studies of azulene and naphthalene on Pt(111) have not been reported. Limited work for the isolated systems was done with low-energy electron diffraction (LEED)<sup>27-30</sup>, temperature-programmed desorption (TPD)<sup>28-29</sup> and scanning tunneling microscopy (STM).<sup>31-33</sup> Work function (WF) measurements,<sup>30</sup> adsorption calorimetry<sup>19</sup> and density functional theory (DFT) calculations<sup>34-35</sup> were until now only performed for naphthalene on Pt(111). For the more weakly interacting Cu(111) surface, it was recently shown that naphthalene is physisorbed, while azulene is chemisorbed,<sup>18</sup> raising the question whether differences in the interaction strength persist when both molecules are strongly chemisorbed.

In this study, we present a comprehensive multi-method comparison of the bonding of naphthalene and azulene to Pt(111). Using SCAC, we measure the first reliable adsorption energies for any non-alternant aromatic molecule on any metal surface and show that it bonds stronger than its alternant isomer. Temperature-programmed desorption (TPD) cannot be applied here, because the molecules do not desorb intact from Pt(111). Details of the chemical bond and the electronic structure are clarified using X-ray and ultraviolet photoelectron spectroscopy (XPS/UPS), near edge X-ray absorption fine structure (NEXAFS) spectroscopy, and WF measurements. DFT calculations including a dispersion-correction scheme (PBE-D3) and applying periodic boundary conditions are used to interpret the experimental data and to gain detailed insight in the underlying mechanisms of the enhanced bonding at the defect/metal interface.

**Figure 1.** (a) Graphene sheet with embedded pentagon-heptagon (5-7) defect (blue). Molecular structures of (b) azulene and (c) naphthalene. The different topologies of the two isomers are illustrated by the color schemes: naphthalene has an alternant topology (only alternating or differently-colored C centers are connected), whereas azulene has a non-alternant topology (two atoms with the same color are connected). As shown in (a), the 5-7 defect locally interrupts the alternant topology of regular graphene.

### RESULTS AND DISCUSSION

Heat of Adsorption Measurements. The most important single parameter in this study is the heat of adsorption as a direct quantitative measure for the strength of the adsorbate-substrate bond. It is defined here as the negative of the differential standard molar enthalpy change for the adsorption reaction,  $-\Delta H_{\rm ads}$ , with the gas having the same temperature as the surface. "Standard" here implies only an ideal gas at 1 bar pressure. Figure 2 shows the

molar heat of adsorption of azulene on Pt(111) at 150 K as a function of coverage. These heats were calculated from the measured absolute calorimetric heats by averaging over five individual measurements, dividing by the number of moles adsorbed in each pulse (given by flux times pulse duration times sticking probability), and adding  $RT_{\text{source}}/2$ , as described previously. No detectable mass spectrometer signal was present due to any non-sticking fraction of the azulene molecular beam, indicating that its sticking probability is always  $\geq 0.995$ . Consequently, both the short and long term sticking probabilities were concluded to be unity.

As described previously, a small enthalpy correction on the measured heat is necessary, because the standard enthalpy of a gas at the temperature of the surface differs slightly from that of the actual experimental molecular beam's gas at this surface temperature.<sup>37</sup> Specifically, the temperature of the source,  $T_{\text{source}}$ , and thus the temperature of the molecules impinging on the sample, is 382 K, which deviates from the sample temperature of 150 K. Therefore, we had to take the additional contribution from the extra thermal energy of the gas molecules into account. We estimated this heat contribution by integrating the experimental heat capacity of the gas  $(C_p)$  vs. T curve<sup>38</sup> between sample and source temperature. The resulting heat, 29 kJ/mol, was subtracted from the directly measured heat. The thus corrected heat of adsorption is plotted versus coverage in Figure 2. It is equal to the standard (1 bar) molar enthalpy of adsorption and the isosteric differential heat of adsorption. Figure 2 shows that the heat of adsorption decreases with coverage. We attribute this decrease to repulsive lateral interactions between the adsorbed azulene molecules. The solid line is a second-order polynomial fit of the experimental data and is described by the equation:

$$\Delta H_{\text{ads}} = (416 - 1370\Theta - 13100\Theta^2) \text{ kJ/mol}$$
 (1)

where  $\Theta$  is the coverage in ML (given as molecules per surface atom, see methods section for a detailed explanation).

The heat of adsorption of naphthalene on Pt(111) was already measured in previous work with the same instrument.<sup>19</sup> To provide a direct comparison with the new data, the old measurements for naphthalene were also fitted with a second-order polynomial and follow the equation:

$$\Delta H_{\text{ads}} = (300 - 330\Theta - 18758\Theta^2) \text{ kJ/mol}$$
 (2)

As can be seen, azulene has a substantially higher heat of adsorption than naphthalene over the whole coverage range, close to that expected for the larger anthracene.<sup>19</sup>

Also shown in Figure 2 is the heat of sublimation of bulk azulene at 150 K. The literature value for the sublimation enthalpy of azulene is  $74.2 \pm 2.2$  kJ/mol at 298 K.<sup>39</sup> This was adjusted to account for the lower temperature of the Pt(111) sample at 150 K by integrating the heat capacities ( $C_p$ ) for gaseous and solid azulene over this temperature range. For gaseous azulene, values are available between 200 and 1000 K.<sup>40</sup> The third-order polynomial fit relating  $C_p$  to temperature was extrapolated to 150 K and integrated between

150 and 298 K. The only available value for  $C_p$  of solid azulene is given at 298 K. <sup>41</sup> To determine the  $C_p$  of solid azulene at a lower temperature, we assessed the solid  $C_p$  values for the similar molecules naphthalene and benzene. The heat capacities for each molecule showed a linear relationship for the entire temperature range of interest, with an average decrease of 50 %  $\pm$  5 % from 298 to 150 K. Consequently, the heat capacity of solid azulene at 298 K was assumed to decrease by 50 % between 298 and 150 K. The resulting linear relationship was integrated over this range. The correction to the sublimation enthalpy of azulene between 150 and 298 K is  $\pm$ 3.92 kJ/mol, resulting in a sublimation enthalpy of 78.1  $\pm$  2.2 kJ/mol at 150 K.

The heat of adsorption of azulene on Pt(111) at 150 K decreased to a relatively constant value of 92.7 kJ/mol between 0.12 and 0.17 ML, when the second layer is growing (with an average heat in this range that varied by  $\pm 3.4$  kJ/mol between runs). Above 0.2 ML, the heat of adsorption reached a nearly constant value which averaged  $80.6 \pm 1.6$  kJ/mol, within error bars of the bulk sublimation enthalpy at 150 K of  $78.1 \pm 2.2$  kJ/mol. The higher heat at coverages in the second layer ( $\sim$ 0.1 to 0.2 ML) indicates that the Pt(111) surface is still close enough to interact with the azulene, in spite of the presence of an intervening layer of adsorbed azulene.

**Figure 2.** Heat of adsorption of azulene on Pt(111) at 150 K as a function of coverage. Blue dots, experimental data; solid black line, fit function of the differential heat; dashed black line, integrated fit function. The dotted line shows the sublimation enthalpy ( $\Delta H_{\text{sub}} = 78.1 \pm 2.2 \text{ kJ/mol}$ ) reported in the literature<sup>39</sup> adjusted for the temperature of 150 K.

Unoccupied electronic states: NEXAFS. The unoccupied frontier orbitals are expected to contribute substantially to the interfacial chemical bond and are probed here with NEXAFS spectroscopy at the carbon K-edge. The resulting spectra for multilayers and monolayers of both molecules on Pt(111) are displayed in Figure 3. In the multilayer regime, the prominent  $\pi^*$  resonance between 283 and 286 eV can be attributed to the 1s  $\rightarrow$  LUMO and 1s  $\rightarrow$  LUMO+1 transitions of the (almost) unperturbed molecules. The energy difference between these two transitions is larger for naphthalene than for azulene, according to previous experimental and theoretical work. As a result, the  $\pi^*$  resonance of naphthalene is split into two peaks, whereas that of azulene only shows one peak with a distinct shoulder on the high-energy side.

In the multilayer, the adsorption edge of azulene appears at a 0.65 eV lower photon energy than that of naphthalene, in line with the lower-lying LUMO of azulene (see below). In the monolayer, this energy difference is reduced to 0.15 eV, because the two isomers respond differently to the presence of the Pt surface: the edge shifts by +0.13 eV for azulene and -0.37 eV for naphthalene. The same edge shifts are also visible in the NEXAFS calculations and can be traced back to the different responses of the unoccupied frontier orbitals to the interaction with the Pt surface (see below).

In the monolayer regime, the broad  $\pi^*$ -resonances of both molecules exhibit a strong dichroism, with a high intensity for grazing incidence of the X-rays (25°), an intermediate

intensity for magic angle incidence (53°), and a low residual intensity for normal incidence (90°). As the  $\pi^*$  orbitals are oriented perpendicular to the molecular plane, it can be deduced that the molecules are lying flat on the surface. The residual intensity of the  $\pi^*$  peaks at normal incidence can be attributed to partial sp<sup>2</sup>-to-sp<sup>3</sup> rehybridization (see below).<sup>42</sup>

The broad  $\pi^*$  resonance shows two maxima in the monolayer spectra of both molecules. In the case of azulene, the first maximum has the higher intensity and the maxima are farther apart (2.4 eV), whereas for naphthalene the second maximum is slightly higher and they are less separated (1.6 eV). How this signal shape arises from a superposition of the various transitions can be seen in the molecular orbital projected NEXAFS calculations (Figure 3cft) provided by DFT. The details of these calculations will be discussed later.

Occupied electronic states: Photoelectron spectroscopy. Further insight into the molecule/metal interface is obtained by probing the occupied electronic states with photoelectron spectroscopy. The core level C 1s spectra for the monolayers of both molecules are shown in Figure 4a. The peaks of the monolayers are shifted by less than 0.1 eV relative to their multilayer positions as indicated by the dotted lines (see Figure S1 in the SI for the multilayer spectra). As can be seen, the monolayer signals show an asymmetric peak shape. The asymmetry of the peaks is an indication for the hybridization of the molecular orbitals with the surface and the presence of molecular electron density around the Fermi edge. In previous work, a similar asymmetric shape of the C 1s peak was observed for azulene on Cu(111), which forms a chemisorptive bond, while it was not found for naphthalene on Cu(111), which is physisorbed. The asymmetry is also absent from the corresponding multilayers peaks (see Figure S1 in the SI).

**Figure 3.** Carbon K-edge NEXAFS data for azulene and naphthalene on Pt(111). Top: experimental spectra of azulene (blue) and naphthalene (red): (a) multilayers, (b) monolayers. The multilayer spectra were taken with the electric field vector oriented 53° relative to the surface normal, the monolayer spectra with the angles indicated by the color scheme (25°, bold color; 53°, intermediate color; 90°, faint color). Center and bottom: MO projection analysis of the DFT calculated NEXAFS spectra of (c,d) the free molecules<sup>18</sup> and (e,f) the monolayers on Pt(111). Contributions of the LUMO in dark red and of the HOMO in dark blue, higher/lower orbitals in incrementally lighter colors, total spectrum in black. The calculated spectra were rigidly shifted by -6 eV to match the experimental energy scale.

The differences between the two monolayer peaks are highlighted in the difference spectrum in Figure 4a (bottom). The azulene peak appears at a slightly higher binding energy and has a larger width. After careful normalization, the intensity of the azulene signal was found to be larger by 7 to 15% depending on the method of background correction. This difference is due to the higher adsorption energy and a more favorable packing of the azulene molecules (see Figure S2 in the SI).

**Figure 4.** Photoemission spectra for azulene and naphthalene on Pt(111). (a) C 1s XP monolayer spectra of azulene (Az, blue) and naphthalene (Nt, red) together with a difference spectrum (Az minus Nt, black). The peak positions and the shifts from the multilayer positions (see multilayer spectra in Figure S1 in the SI) are indicated by dotted lines above the peaks. (b) He-I UP spectra: Top, monolayers and clean Pt(111) surface (black); bottom, multilayers and DFT orbital energies (vertical lines). The orbital energies from DFT were modified to match the experimental energy scale as described in detail in the SI and in the literature. 44-45

UPS was used to probe the occupied valence states. In Figure 4b, the multilayer and monolayer spectra of both molecules are compared to the spectrum of clean Pt(111). The orbital energies indicated by vertical lines were obtained by gas phase DFT calculations (PBE/def2-TZVPP) and can be found in Table S1 in the SI. The energy axis of these DFT results was shifted and scaled by a factor of 1.2 to match the experimental peaks of the multilayer spectra, a procedure that as was already reported for similar systems. The orbital energies are then in good agreement with the experimental peaks and literature values obtained using a more sophisticated theoretical method.

In the multilayer spectra, the energetic positions of the orbitals reflect the different electronic structures of the (approximately undisturbed) molecules. The HOMO related UPS signal of azulene appears 0.63 eV higher in energy (2.49 eV below  $E_{\rm F}$ ) than that of naphthalene (3.12 eV below  $E_{\rm F}$ ). These HOMO energies determine, together with the LUMO energies, the electronic band gaps of the molecules. The absolute LUMO energies are experimentally not directly accessible with our methods. However, the NEXAFS spectra in Figure 3a provide the difference between the LUMO energies of the two molecules. This is possible because of the almost identical multilayer C 1s peak positions of both molecules (Figures 4a and S1), which indicate that the energy difference of the  $\pi^*$ resonances is exclusively caused by the different LUMO energies. The LUMO related feature of azulene appears here at 0.65 eV lower photon energy than that of naphthalene. The energy differences of the HOMOs and LUMOs directly show that the electronic gap is 1.28 eV smaller for azulene than for naphthalene. This value is in excellent agreement with the electronic band gap difference obtained from ionization energy and electron affinity of the gas-phase molecules, which is also 1.3 eV. 47 The difference of the orbital energies of HOMO and LUMO as calculated by DFT is 1.37 eV, which additionally supports our approach. Note that this electronic gap is quite different from the optical gap. The optical gaps of naphthalene and azulene have a much larger difference of 2.37 eV.<sup>48</sup>-<sup>49</sup> The reason for this deviation is the non-alternant character of the azulene molecule. It causes not only the reduced HOMO-LUMO gap, but also leads to a stronger localization of the frontier orbitals, resulting in reduced electron-electron repulsion in the excited state and thus in a smaller optical gap.<sup>47</sup>

In the monolayer spectra, various molecule-induced features can be identified, although most are strongly superimposed by the Pt d-band between the Fermi edge ( $E_F$ ) and 6 eV below  $E_F$ . Naphthalene shows a higher intensity close to  $E_F$ , which may be due to weaker attenuation of the Pt d-band by this less strongly interacting molecule. Azulene has a higher intensity around 4 eV at the second peak of the Pt d-band. Both molecules induce enhanced intensity between 2 and 3 eV and a distinctive pattern of lower lying molecular orbitals from 7 to 11 eV, which are shifted by 0.7 eV relative to their multilayer positions.

A molecular orbital (MO) projection scheme for the DFT calculated density of states (DOS; discussed in detail below) shows a considerable contribution of the carbon states to the DOS between 2 and 3 eV. It is even possible to identify the mainly contributing orbitals in this energy range. These orbitals are the LUMO and LUMO+1 for naphthalene and the HOMO, LUMO and LUMO+1 for azulene.

He-I UP spectra for a wide coverage range of both molecules on Pt(111) are shown in Figure 5a,b. It can be seen how the d-band of the metal surface is quickly attenuated (downward arrows) and that the molecular states of the multilayers appear at higher coverages (upward arrows). The shift of the secondary electron cut off indicates the lowering of the work function with increasing coverage. The resulting WF changes are plotted in Figure 5c and will be discussed in detail below.

Work function changes. In Figure 5c, the experimental WF changes as extracted from the He-I UPS data are plotted as functions of the coverage. Adsorption-induced changes of the electronic WF of the surface are related to the vertical dipole moment of the adsorbate-substrate complex. The WF data were analyzed using the Topping model,<sup>50-51</sup> which provides the unattenuated dipole moment per molecule  $\mu_0$  and the polarizability volume  $\alpha$  of the adsorbate complex. The results of these fits are summarized together with the WF changes at a coverage of 0.11 ML in Table 1 and compared to the values calculated by DFT. The DFT-calculated WF changes at several other coverages are presented in Figure S3 in the SI.

**Figure 5.** Coverage dependent He-I UPS data for (a) azulene and (b) naphthalene on Pt(111). The spectra are colored according to their coverage with a scale from red (clean surface) to purple (0.45 ML) in the order of the spectral colors. The downward arrows indicate the attenuation of the substrate signals, while the upwards arrows indicate the growing of the molecule-related multilayer signals. (c) Coverage dependence of the experimental work function (WF) changes  $\Delta\Phi$  (symbols) and fits with the Topping model (solid lines). Blue and open circles, azulene; red and open diamonds, naphthalene.

**Table 1.** Experimental (Expt.) and theoretical (DFT) work function (WF) data for azulene and naphthalene on Pt(111):  $\Delta\Phi$ , WF changes for a coverage of 0.11 ML;  $|\mu_0|$ , unattenuated dipole moment per molecule;  $\alpha$ , polarizability volume. The experimental  $|\mu_0|$  and  $\alpha$  values

were extracted from the WF change data using the Topping equation.<sup>50-51</sup>  $|\mu_0|$  (DFT) was obtained by fitting a modified Topping equation directly to the DFT calculated dipole moments of the six investigated coverages. Details of the fitting procedures can be found in the SI.

	azulene/Pt(111)	naphthalene/Pt(111)
ΔΦ (Expt.) / eV	-2.09	-2.08
$\Delta\Phi$ (DFT) / eV	-2.43	-2.52
$ \mu_0 $ (Expt.) / D	6.80	6.30
$ \mu_0 $ (DFT) / D	5.99	6.03
$\alpha \left( \text{Expt.} \right) / 10^{-29}  \text{m}^3$	3.62	3.23

The work function change at monolayer coverage is almost the same for both molecules (-2.09 and -2.08 eV). The result for naphthalene is in reasonable agreement with a previous reported value of  $\Delta\Phi$  = -2.0 eV on Pt(111).<sup>30</sup> Azulene shows a slightly steeper trace in the first few points of the work function change, thus the Topping fit yields slightly larger values for  $|\mu_0|$  (6.80 vs. 6.30 D) and  $\alpha$  (3.62 vs. 3.23·10<sup>-29</sup> m³).

The lowering of the work function and the extracted dipole moment cannot be attributed to the charge transfer between surface and molecule. The DFT calculations presented below show that there is a complicated system of bonding and back-bonding, but the net charge transfer is from the surface to the molecule, as also visible in the NEXAFS measurements and calculations. The resulting charge transfer dipole therefore has the negative end at the molecule and would lead to an increased work function. Instead, the lowering of the work function and the build-up of the dipole moment are due to the so called Pauli-pushback effect<sup>52-53</sup>, which describes the redistribution of electron density near the surface due to the Pauli-repulsion with the electrons in the molecule.

Density-functional theory (DFT) calculations. DFT calculations were performed on the generalized-gradient approximation level of density functionals (PBE) using periodic boundary conditions (PBC) and a dispersion-correction scheme (DFT-D3). To account for coverage-dependent effects, six different supercells were chosen. The smallest was the (3×3) structure (highest coverage, 0.111 ML) and the largest was the (7×7) structure (lowest coverage, 0.020 ML).

Structures. The optimized (3×3) structures of azulene and naphthalene on Pt(111) are shown in Figure 6. Both molecules favor adsorption with the bridging bond on top of a Pt atom. The long molecular axis of naphthalene is aligned with the [110] direction of the surface (Figure 6b), whereas azulene is azimuthally rotated by 11° with respect to this axis (Figure 6a). The adsorption site of naphthalene agrees with that in previous theoretical studies, 34-35 while there is no related previous work for azulene.

The overall adsorption height, i.e., the vertical distance of the carbon atoms above the relaxed Pt(111) surface plane, is quite similar for azulene and naphthalene with 2.09 Å and 2.08 Å, respectively. This similarity is quite remarkable, considering the different adsorption energies and the fact that a height difference of 0.62 Å was calculated on Cu(111) using the same method. 18 For naphthalene, previous DFT studies (without dispersion correction schemes) reported larger adsorption heights of 2.25 Å<sup>35</sup> and 2.15 Å<sup>34</sup>. The adsorption height is nearly independent of the coverage and is constant within ±0.01 Å for all coverages mentioned above (see Figure S4 and Table S3 in the SI). A coverage dependence of the adsorption height is often observed for weakly bonded systems, 54 for which the molecule-surface potential is soft and thus an elongation of the adsorption bond with increasing coverage can alleviate the lateral intramolecular repulsion. The potentials of the vertical and lateral interaction are therefore coupled and influence each other. In the strongly chemisorbed systems of azulene and naphthalene on Pt(111), however, the vertical potential is steep and couples less with the lateral repulsion potential. Therefore, the vertical distances are more stable and less affected by the lateral repulsion (and thus by the coverage). A detailed of discussion of the adsorption heights with respect to the chosen reference system can be found in the SI.

The strong interaction with the Pt(111) surface leads to a drastic deformation of molecule and surface (Figure 6c,d). The deformation follows different patterns for azulene and naphthalene, which can be understood as different manifestations of the balance between two bonding mechanisms: (1) the formation of a delocalized bond between surface and the  $\pi$ -electron system of the molecule ( $\pi$ -bonding case) and (2) the formation of localized bonds between surface atoms and single carbon atoms in the molecule ( $\sigma$ -bonding case).

Both molecules undergo in-plane (Figure 6e,f) and out-of-plane deformation (Figure 6c,d). The out-of-plane tilting of the C-H bonds is pronounced for both molecules, indicating the rehybridization from  $sp^2$  to  $sp^3$ . The tilt angle is dependent on the  $\alpha$ - or  $\beta$ -positioning of the hydrogen atoms for naphthalene, while for azulene the hydrogen atoms at the 5-membered ring show a larger tilt. A more detailed analysis of the bond lengths and angles in the adsorbate structure is presented in the SI.

Adsorption of naphthalene on Pt(111) leads to an elongation of all C-C bonds, in agreement with the transition from conjugated bonds between  $\rm sp^2$  carbon atoms in the free molecule towards single bonds between  $\rm sp^3$  carbon atoms in the adsorbed state (Figure 6f). In the case of azulene, however, the bridging bond gets shorter by -4.1 pm upon adsorption, indicating its increased double-bond character (Figure 6e). The unusual shortening of this bond can be explained by the donation of charge into the former LUMO of the molecule, which is  $\pi$ -bonding with respect to the bridging bond, as was previously discussed for adsorption on Cu(111).<sup>18</sup>

The out-of-plane deformation of the adsorbed molecules limits their suitability as model systems for structural motifs of graphene, because the rigid 2D structure of the graphene sheet makes a distortion similar to the one observed for the molecules impossible. This rigidity hinders the rehybridization to sp<sup>3</sup> and limits the charge that can be transferred

between graphene sheet and surface. The rigidity therefore may also be the reason behind the large adsorption height of the graphene sheet on Pt(111), which is 3.1 to 3.2 Å.<sup>55</sup> Nevertheless, because the azulene molecule shows a larger adsorption energy than naphthalene, while having the same adsorption height, an enhanced interaction of the 5-7 defects with the Pt(111) surface is still likely. Another difference between the molecules and a graphene sheet is the registry with the Pt(111) surface, which leads to different adsorption sites for different parts of the graphene sheet and also different possible adsorption sites for the defects. However, we calculated structures and energies of the molecules adsorbed on several adsorption sites and azulene always showed the stronger interaction (Table S4 of the SI).

**Figure 6.** DFT optimized structures of the (3×3) supercell of azulene (left) and naphthalene (right). (a,b) Top view, (c,d) side view and average (avg.) out-of-plane angles as indicated by the color scheme (see the text for further details). (e,f) Changes of the bond lengths relative to the gas phase-optimized structure (in pm), (g,h) vertical displacements (in pm) of the platinum atoms in the topmost layer, compared to the relaxed surface without a molecule. Positive values mean a displacement towards the molecule.

The adsorption-induced in-plane bond-length changes can also be discussed in the context of aromaticity. The aromatic character of a molecule can be quantified by the harmonic oscillator model of aromaticity (HOMA),<sup>56</sup> which is based on the molecular geometry. The detailed HOMA analysis for azulene and naphthalene on Pt(111) can be found in the SI (see Figure S5). In short, the hybridization between molecular orbitals and electronic states of the surface lifts the distinction between the annulenoid aromaticity of azulene and the benzenoid aromaticity of naphthalene present in the gas phase structures.

The adsorption-induced deformation of the first Pt surface layer is visualized in Figure 6g,h. Both molecules push the atom beneath the bridging bond deeper into the surface. Naphthalene pulls the six neighboring atoms uniformly above the plane, whereas azulene exerts a stronger pull on the four atoms parallel to its long axis and a lesser pull on the atoms in coaxial positions. The overall range of the surface deformation (vertical distance between highest and lowest surface atom) is larger for azulene (31 pm) than for naphthalene (24 pm), in line with its stronger bond to the surface.

Charge density difference plots. The adsorption of azulene and naphthalene on Pt(111) is accompanied by massive charge redistribution, as revealed by the charge density difference plots in Figure 7. The depletion of charge (red) in the first surface layer and the accumulation of charge (blue) between molecule and surface as well as on the molecule are clearly visible.

**Figure 7.** Charge density difference plots of azulene (left) and naphthalene (right) on Pt(111). (a,b) Top views, (c,d) side views. The isosurface value is 0.007 e<sup>-</sup>/Å<sup>3</sup> for all plots, blue, electron accumulation; red, electron depletion.

Electron depletion in the first Pt surface layer is visible as dumbbell-shaped regions (red) centered at the surface Pt atoms. These shapes suggest that the transfer of electron density to the molecule may be mediated by the Pt p-orbitals. This assumption seems reasonable, considering the presence of an occupied 6p-related surface state close to  $E_F$ . The p-orbital type features and the corresponding spatial regions of electron accumulation in the molecule have the overall shape of a localized  $\sigma$ -type bond, as would be expected for a sp<sup>3</sup> hybridized carbon atom. Depending on the position of a surface Pt atom relative to the C atoms in the molecule, the C-Pt bonds show different types of localization and different influences on the molecular geometry. If a surface atom is close to a C atom, the bond is directed at this atom, the nearby C-C bonds are elongated, and the tilt of the C-H bond indicates substantial sp<sup>3</sup> character. In contrast, if the surface Pt atom is close to a C-C bond, electron density is accumulated close to the bond, while out-of-plane C-H tilt and C-C bond elongation are less pronounced.

Charge Transfer. The charge transfer between molecule and substrate was quantified using several different charge portioning schemes, including Hirshfeld charge analysis,  $^{58}$  iterative Hirshfeld charge analysis,  $^{59-61}$  Bader's atoms in molecules (AIM) charge analysis,  $^{62}$  and integration of the molecular DOS up to  $E_{\rm F}$ . The results obtained by the different methods vary substantially (see Table S5 in the SI). Even the direction of the total charge transfer is not the same for all methods, but the majority of the methods predicts surface-to-molecule charge transfer. The conflicting results are hinting towards a charge-transfer mechanism involving donation from the surface to the molecule as well as from the molecule back to the surface, resulting in partial compensation. Using the pEDA method, we will further investigate this mechanism below.

Work function changes and dipole moments. Comparison of the calculated WF changes  $\Delta\Phi$  at monolayer coverage with the experimental results in Table 1 shows that theory overestimates  $\Delta\Phi$  by 0.34 eV for azulene and 0.44 eV for naphthalene. The calculated data for all other coverages are compiled in Figure S3 in the SI and show better agreement for smaller coverages. The slightly larger WF change induced by naphthalene may result from its smaller adsorption height, because the WF change is partly caused by the Pauli-push back effect, which is known to depend on the adsorption height. <sup>18</sup>

Independently of the WF changes, DFT also yields coverage-dependent vertical dipole moments  $\mu$ , which were fitted with a modified Topping equation to obtain theory values for the unattenuated dipoles  $\mu_0$  (see the SI for details). Comparison with the experimental  $\mu_0$  values (Table 1) shows deviations of only 12% for azulene and 4% for naphthalene. The substantial vertical dipole moments may partly result from the out-of-plane deformation of

the molecules, but it is not possible to quantify this contribution (see detailed discussion in the SI, Table S2).

Molecular-orbital projection scheme. Analysis of the valence electronic structure of the adsorbed molecules by a MO-projection scheme reveals substantial adsorption-related broadening and changes of the energetic position of the frontier orbitals (Figure 8). Both molecules engage in massive hybridization of unoccupied and occupied orbitals with metal states. As a result, occupied (unoccupied) orbitals of the free molecules contribute to the DOS above (below)  $E_F$  in the adsorbed state, leading to a partial occupation of both types of orbitals. For example, the HOMOs of azulene and naphthalene are filled by only 1.8 electrons in the adsorbed state (instead of 2), whereas the former LUMOs are occupied by 1.6 electrons in both adsorbed molecules.

**Figure 8.** Total density of states (TDOS) and MO-projected density of states of the adsorbed molecules on Pt(111) for (a) azulene and (b) naphthalene. Contribution of the LUMO in dark red and of the HOMO in blue; higher/lower orbitals in incrementally lighter colors, total DOS (scaled for better presentation) in black. The lines in the center denote the gas-phase orbital energies, which have been shifted to maximally align the lowest-lying states of the gas phase and the adsorbed molecule.

NEXAFS calculations. The theoretical analysis of the NEXAFS spectra shown in Figure 3a and 3b is based on MO-projections for the DFT calculated transitions. The first  $\pi^*$ resonance of the free molecules comprises contributions from the C1s → LUMO and C1s → LUMO+1 transitions, as shown in Figure 3c and 3d. In the adsorbed state, all MO contributions are reduced, because hybridization of the molecule with metal bands makes states with dominant metallic character also contribute. In addition, the contributions of LUMO and LUMO+1 are attenuated compared to the other orbitals and shifted in energy. The onsets of the  $\pi^*$  peaks shift by +0.29 eV (azulene) and -0.41 eV (naphthalene), in good agreement with the experimental values of +0.13 and -0.37 eV, respectively. The MOprojections, however, reveal that the LUMOs of both molecules are elevated to higher energies. The downshift of the onset of the naphthalene spectrum is caused by the emergence of the new C1s → HOMO transition and the broadening of all peaks. The LUMO peak shift for azulene is larger and overcompensates the effect of the broadening. The better accessibility of the low-lying LUMO of azulene may be the key for the understanding of its stronger bond to the metal surface, in line with previous observations for adsorption on Cu(111).18 In addition to intensity stemming from the unoccupied orbitals, contributions from the formerly fully occupied HOMO and HOMO-1 appear, in accord with the reduced occupation of these orbitals as deduced from the MO-projected DOS. The broad spectral features of the first transitions of both molecules include now transitions belonging to a multitude of final-state orbitals, in contrast to the free-molecule or multilayer cases, where the first transition is related only to the LUMO and LUMO+1. In the case of adsorbed azulene, the first peak comprises contributions of the HOMO-1,

HOMO, LUMO and LUMO+1, while the second peak stems from LUMO+2 and LUMO+3 contributions. Both peaks contain additional contributions from metallic conduction bands. For adsorbed naphthalene, the LUMO+2 peak shifts to lower energies, reducing the dip between the peaks as seen in the experimental spectra (Figure 3b).

Adsorption energies. DFT calculations of adsorbed large organic molecules are often performed for only one, rather high coverage to reduce the unit cell size and thus the computational effort. This restriction ignores the coverage dependence of many properties, including the adsorption energy. For comprehensive comparison with the coverage-dependent SCAC data, we calculated six different adsorbate structures in wide range of coverages.

The DFT adsorption energies for the lowest calculated coverage ((7×7) structure, coverage of 0.020 ML) are -389 kJ/mol for azulene and -345 kJ/mol for naphthalene. These values decrease to -308 kJ/mol and -258 kJ/mol at the highest coverage ((3×3) structure, 0.111 ML). The adsorption energies for all calculated structures are compared to the experimental SCAC values in Figure 9. The SCAC data for naphthalene are taken from the literature.<sup>19</sup>

For a meaningful comparison of the integral electronic adsorption energies from theory with the differential experimental energies, the second order polynomials obtained by fitting the experimental data were integrated. For a coverage of 0.083 ML, harmonic zero-point vibrational energy (ZPVE) and harmonic thermodynamic corrections for the DFT-derived values were performed, yielding the adsorption enthalpy in addition to the electronic adsorption energy directly produced by DFT.

For azulene, the calculated and measured adsorption energies agree remarkably well and deviate by an average of only 8 kJ/mol over the coverage range. In contrast, the adsorption energy of naphthalene is overestimated by an average of 53 kJ/mol. An overestimation by theory is expected, since the D3 dispersion correction is known for this shortcoming. <sup>18, 63-64</sup> In previous work, DFT-D3 overestimated the adsorption energies of azulene and naphthalene on Cu(111) by 28 kJ/mol and 45 kJ/mol, respectively. <sup>18</sup> Considering the finite temperature of the measurements, neglecting anharmonicities in the calculations may additionally contribute to this overestimation: The vertical potential of the molecule on the surface is strongly anharmonic, resulting in an increased adsorption height and decreased adsorption energy at elevated temperatures. <sup>65</sup> The literature SCAC data for naphthalene were measured at 300 K, <sup>19</sup> whereas the SCAC data for azulene in this work were measured at 150 K. Therefore, the lowering effect of the elevated temperature on the adsorption energy by should be stronger for naphthalene. It is, however, impossible to distinguish between these effects and the inherent limitations of DFT-D.

**Figure 9.** Integral adsorption energies for azulene (blue) and naphthalene (red) on Pt(111). Experiment (Expt., dashed lines): Second-order polynomials for the measured integral heats of adsorption taken from Figure 2 (azulene) and the literature (naphthalene). Theory: Adsorption energies for the six coverages calculated on the PBE-D3 level (open

circles). Also included are previous DFT results for naphthalene (triangles<sup>35</sup> and diamond<sup>34</sup>). The corrected DFT values for the coverage of 0.083 ML (ZPVE and enthalpies) are plotted in progressively lighter colors (filled circles, overlapping).

The calculations correctly reproduce the higher adsorption energy of azulene and the general coverage dependences for both isomers. Considering their almost identical adsorption heights, it may be concluded that the latter (and the WF changes) are mainly determined by Pauli-repulsion, whereas the extra adsorption energy of azulene is structurally mainly expressed in the larger deformations of the molecule and the surface. However, the theoretical adsorption energies of the two isomers differ by 37 to 50 kJ/mol over the whole coverage range, which is distinctively smaller than the experimental difference of 85 to 116 kJ/mol. The harmonic zero-point vibrational and thermodynamic corrections change the adsorption energy only slightly to larger values (ZPVE: 1-2 kJ/mol, thermodynamic corrections 5-7 kJ/mol). As shown in the bottom part of Figure 9, previous theoretical studies without dispersion corrections strongly underestimated the adsorption energy of naphthalene on Pt(111).<sup>34-35</sup> These deviations illustrate that dispersion corrections are also necessary in the case of chemisorption.<sup>64</sup> In our case, the dispersion attraction accounts for approximately one third of the interaction energy, as discussed in the SI.

Energy decomposition analysis: The energy decomposition analysis for extended systems (pEDA) interprets the adsorbate-substrate bond by quantifying the various contributions to the adsorption energy. For this purpose, the system is split up into two fragments representing the molecule and the surface. The total interaction energy between these fragments can then be divided into different terms to obtain detailed information on the surface chemical bond.  $^{66-67}$  The complete pEDA data set for azulene and naphthalene on Pt(111) can be found in Table S6 of the SI. Using the natural orbitals for chemical valence (NOCV) extension to the pEDA, it is possible to subdivide the orbital interaction into deformation densities  $\Delta \rho_i$ , each being a specific charge rearrangement with an assigned energy term.  $^{67-68}$  As one fragment is a metal surface, the situation is more complex than for molecular systems and many NOCVs contribute to the overall orbital interaction. However, the fundamental bonding situation can be traced back to few dominant contributions.

The overall bonding mechanisms are similar for both molecules, including pronounced contributions from surface-to-molecule and molecule-to-surface flows of electron density, in analogy to the Dewar-Chatt-Duncanson model.<sup>69</sup> Exemplary deformation densities for both bonding and back-bonding are presented in Figure 10 for azulene. The full data set of the NOCV analysis is presented in the SI. The ten most important NOCV deformation densities for both molecules are shown in Figures S6 and S7, while the corresponding energies are compiled in Tables S7 and S8.

**Figure 10.** Selected representative NOCV deformation densities for azulene on Pt(111). Red, electron depletion; blue, electron accumulation. (a) Deformation density showing electron transfer from the molecule to the surface, isosurface value: 0.003 e<sup>-</sup>/Å<sup>3</sup>. (b) Deformation density showing electron transfer from the surface to the molecule, isosurface value: 0.001 e<sup>-</sup>/Å<sup>3</sup>. Eigenvalues v in units of e, energies in units of kJ/mol.

#### **CONCLUSIONS**

The isomers azulene and naphthalene constitute a versatile molecular model system to study interfacial interactions of the topological pentagon-heptagon (5-7) defects in graphene. The experimental and theoretical analysis reveals that both molecules are chemisorbed on Pt(111), but azulene forms the stronger bond. Its differential adsorption energy, as measured by SCAC, is larger by 68 to 116 kJ/mol, depending on the coverage, and reaches 416 kJ/mol at zero coverage, compared to 300 kJ/mol for naphthalene. The stronger bond of azulene and the coverage dependencies of the adsorption energies are qualitatively correctly predicted by dispersion-corrected DFT calculations. DFT reveals rehybridization towards sp<sup>3</sup> and a partially localized  $\sigma$ -character of the molecule-metal bond. The interfacial electron transfer occurs in both directions through donation and backdonation, resulting in the partial occupation (deoccupation) of orbitals that are unoccupied (occupied) in the free molecules, as shown by pEDA. Interpretation of the UP and NEXAFS spectra with an MO-projection analysis supports the occupation/deoccupation mechanism of the surface chemical bond. It also reveals that the molecular orbitals of azulene and naphthalene respond differently to adsorption. This observation connects the topology-related differences in the electronic structure (especially the HOMO-LUMO gap) with the different bonds to the surface. Our analysis shows that the  $\pi$ -topology of an aromatic ring system substantially influences its interaction at a metal/organic interface in the regime of strong chemisorption. Topology-related effects are therefore relevant for various applications, including metal/organic interfaces in organic (opto)electronic devices or catalytic reactions of aromatic hydrocarbons on transition-metal surfaces.

# **METHODS**

Experimental Methods. The adsorption of azulene and naphthalene on Pt(111) was studied under ultra-high vacuum (UHV) conditions at base pressures below  $2 \times 10^{-10}$  mbar.

Azulene (Sigma-Aldrich, purity >99.0 %) and naphthalene (Sigma-Aldrich, purity >99.7 %) were introduced into the vacuum systems through leak valves after initial pump-freezethaw cycles of the reservoirs, or (for calorimetry) by extensive pumping of the vapor to remove impurities. The polished Pt(111) single-crystal surface (purity >99.999 %, roughness < 0.01  $\mu$ m, orientation accuracy < 0.4°, from MaTecK/Germany) was prepared by iterated cycles of sputtering with Ar<sup>+</sup> ions (1 keV, 15  $\mu$ A, 30 min), O<sub>2</sub> treatment (5·10<sup>-7</sup> mbar, 750 K, 30 min), and flash annealing (1100-1300 K). Surface cleanliness and structure were confirmed by XPS, LEED and STM. Sample temperatures were measured with a type

K thermocouple directly mounted to the single crystal. Coverages are given in the unit monolayer (ML) defined as the number of molecules per platinum atom in the Pt(111) surface (atomic density of the Pt(111) surface: 1.50·10<sup>19</sup> m<sup>-2</sup>). If a "full monolayer" is mentioned, this corresponds to one complete layer of molecules on the surface (which corresponds to 0.111 ML for azulene).

XPS and UPS were performed with a PHOIBOS 150 electron energy analyzer equipped with an MCD-9 multi channeltron detector. For XPS, monochromatic Al- $K_{\alpha}$  radiation from a SPECS XR 50 M X-ray anode with a FOCUS 500 monochromator was employed. He-I UP spectra and work functions were measured with a UVS 10/35 gas discharge lamp.

NEXAFS spectroscopy was performed at the synchrotron radiation facility BESSY II (Helmholtz-Zentrum Berlin) using the HE-SGM dipole beamline, which provides linearly polarized radiation with a polarization factor of 0.91 and an energy resolution of 300 meV at the carbon K-edge. The partial electron-yield (PEY) mode was used with a retarding field of -150 V and a channeltron detector voltage of 2.2 keV. Further information on the data treatment can be found in the SI.

The SCAC experiments were performed in a UHV chamber equipped with facilities for XPS, LEED, Auger electron spectroscopy (AES), and low-energy ion scattering spectroscopy (LEIS). The apparatus and procedures for SCAC have been described in extensive detail previously.<sup>38, 70-71</sup> Briefly, the Pt(111) samples used in the SCAC experiments are 1 µm thick single-crystal foils and were provided by Jacques Chevallier at Aarhus University. The sample was cleaned by gentle Ar<sup>+</sup> sputtering followed by repeated cycles of O<sub>2</sub> treatment at 10<sup>-6</sup> mbar and 873 K and annealing at 1123 K in UHV. After this treatment, impurities were below the Auger and XPS detection limits, and LEED showed the spots expected for Pt(111). The heats of adsorption and sticking probability were measured simultaneously as a pulsed molecular beam of azulene was dosed onto the Pt surface. The molecular beam was created by expanding azulene vapor (0.2 - 0.9 mbar)through a glass capillary array, collimating it through a series of five orifices that are cooled with liquid nitrogen, and then chopping into 102 ms pulses. The heats were measured with a pyroelectric ribbon gently pressed on the backside of the Pt crystal. The sticking probabilities were measured with a quadrupole mass spectrometer (QMS) using the King and Wells method.<sup>72</sup>

Density Functional Theory Calculations. DFT calculations applying periodic boundary conditions were performed using the Vienna Ab Initio Simulation Package (VASP)<sup>73-76</sup> with the generalized gradient approximation (GGA) proposed by Perdew, Burke, and Ernzerhof (PBE)<sup>77</sup> for the exchange-correlation functional in combination with the D3 vander-Waals correction scheme with Becke-Johnson-type damping,<sup>78-79</sup> and the projector-augmented wave (PAW) ansatz<sup>80-81</sup> for the atomic cores. A plane-wave cutoff energy of 350 eV and a vacuum layer of 30 Å were chosen. For all calculations a 24×24×1 Monkhorst-Pack k-point mesh was adjusted to the supercell of the 4-layer slab, leading to an 8×8×1 k-mesh for the (3 × 3) supercell.

X-ray absorption spectra were calculated using the pseudopotential plane-wave code CASTEP-18.1.<sup>82</sup> For the XPS shifts the delta self-consistent field (DeltaSCF) method of constraining electronic occupations to resemble full core-hole excitations was used. NEXAFS spectra were calculated using on-the-fly generated USPPs and the CASTEP module ELNES<sup>83</sup> and the transition-potential approach.<sup>84-85</sup> For more details on the computational settings and analysis see the SI and Diller *et al.*<sup>86</sup> For more details on the implementation of the molecular orbital projection method, see Maurer and Reuter.<sup>87</sup>

The energy decomposition analysis using periodic boundary conditions (pEDA) was performed in ADF-BAND 2018.105 using the PBE functional and the DFT-D3 dispersion correction scheme,  $^{77-78, 88}$  a TZ2P basis set  $^{89-90}$  and considering relativistic effects with the zeroth order regular approximation (ZORA),  $^{80-81, 91}$  with the pEDA as implemented in the ADF-BAND package  $2018^{66, 92-93}$ . The optimized ( $2\sqrt{3} \times 2\sqrt{3}$ )R30° structures were taken from the PBE-D3 calculations in VASP, in ADF-BAND a  $7\times7$  k-grid and 2-dimensional periodic boundary conditions were used.

The pEDA method allows to decompose the bond energy into several physically welldefined terms, thus permitting a more detailed interpretation of the character of the chemical bond between two fragments.<sup>67</sup> In our case the fragments are chosen to be the molecule and the surface in their respective singlet electronic states. The convergence of the pEDA values with the k-space sampling density is non-trivial for metal surfaces<sup>66</sup> and has been checked thoroughly (see Table S9 of the SI). The NOCV extension of the pEDA method also allows to decompose the orbital interaction term  $\Delta E_{\rm orb}$  into its constituent subterms. In this scheme the electron density difference  $\Delta \rho$  caused by the orbital interaction can be expressed by a set of fragment orbitals. All of these fragment orbitals are paired according to their matching eigenvalues of  $\pm v_i$ . They can be discussed very instructively in the form of their deformation densities  $\Delta \rho_i$ . Each deformation density shows the electron flow caused by the formation of the interaction between the corresponding pair of fragment orbitals and can be connected to the energy gained and the charge transferred (which equals the eigenvalue v<sub>i</sub> of the deformation density). Because of technical restriction of the method, the calculations for the NOCV extension of pEDA were performed only for the  $\Gamma$ point, the difference in the regular pEDA terms is small and discussed in Table S10 of the SI. Further details for all DFT calculations can also be found in the SI.

#### ASSOCIATED CONTENT

#### **Supporting Information.**

The Supporting Information is available free of charge on the ACS Publications website at DOI: xxxx. Details of the NEXAFS data treatment, XPS multilayer data, DFT orbital energies, additional information about the packing in the molecular layer, details of the Topping fits of the work function analysis, coverage dependence of the adsorption heights, HOMA model, pEDA, and miscellaneous technical details of the DFT calculations. (PDF)

#### **AUTHOR INFORMATION**

## **Corresponding Author**

\*michael.gottfried@chemie.uni-marburg.de

#### **Notes**

The authors declare no competing financial interest.

#### **ACKNOWLEDGMENT**

Funded by the Deutsche Forschungsgemeinschaft (DFG, German Research Foundation) through 223848855-SFB 1083. We thank the synchrotron radiation facility BESSY-II of the Helmholtz-Zentrum für Materialien und Energie, Berlin, for allocation of beam time at the HE-SGM beamline and financial support. We thank Lukas Hellweg for assistance during the spectroscopy measurements. We further acknowledge computational resources from HRZ Marburg, Goethe-CSC Frankfurt and HLR Stuttgart. SJH and RJM acknowledge funding for a PhD studentship through the EPSRC Centre for Doctoral Training in Molecular Analytical Science (EP/L015307/1) and computing resources via the EPSRC-funded HPC Midlands+ computing centre (EP/P020232/1) and the EPSRC-funded Materials Chemistry Consortium for the ARCHER UK National Supercomputing Service (EP/R029431/1). RJM acknowledges support via a UKRI Future Leaders Fellowship (MR/S016023/1).

#### **REFERENCES**

- 1. Geim, A. K.; Novoselov, K. S. The Rise of Graphene. *Nat. Mat.* **2007**, *6*, 183-191.
- 2. Kim, P. Across the Border. *Nat. Mat.* **2010**, *9*, 792-793.
- 3. Tsen, A. W.; Brown, L.; Levendorf, M. P.; Ghahari, F.; Huang, P. Y.; Havener, R. W.; Ruiz-Vargas, C. S.; Muller, D. A.; Kim, P.; Park, J. Tailoring Electrical Transport across Grain Boundaries in Polycrystalline Graphene. *Science* **2012**, *336*, 1143-1146.
- 4. Huang, P. Y.; Ruiz-Vargas, C. S.; van der Zande, A. M.; Whitney, W. S.; Levendorf, M. P.; Kevek, J. W.; Garg, S.; Alden, J. S.; Hustedt, C. J.; Zhu, Y., et al. Grains and Grain Boundaries in Single-Layer Graphene Atomic Patchwork Quilts. *Nature* **2011**, *469*, 389-393.
- 5. Yazyev, O. V.; Louie, S. G. Electronic Transport in Polycrystalline Graphene. *Nat. Mat.* **2010**, *9*, 806-809.
- 6. Kim, K.; Lee, Z.; Regan, W.; Kisielowski, C.; Crommie, M. F.; Zettl, A. Grain Boundary Mapping in Polycrystalline Graphene. *ACS Nano* **2011**, *5*, 2142-2146.
- 7. Grantab, R.; Shenoy, V. B.; Ruoff, R. S. Anomalous Strength Characteristics of Tilt Grain Boundaries in Graphene. *Science* **2010**, *330*, 946-948.
- 8. Rasool, H. I.; Ophus, C.; Klug, W. S.; Zettl, A.; Gimzewski, J. K. Measurement of the Intrinsic Strength of Crystalline and Polycrystalline Graphene. *Nat. Comm.* **2013**, *4*, 2811.
- 9. Ito, Y.; Shen, Y.; Hojo, D.; Itagaki, Y.; Fujita, T.; Chen, L.; Aida, T.; Tang, Z.; Adschiri, T.; Chen, M. Correlation between Chemical Dopants and Topological Defects in Catalytically Active Nanoporous Graphene. *Adv. Mater.* **2016**, *28*, 10644-10651.
- 10. Malola, S.; Häkkinen, H.; Koskinen, P. Structural, Chemical, and Dynamical Trends in Graphene Grain Boundaries. *Phys. Rev. B* **2010**, *81*, 165447.
- 11. Wei, Y.; Wu, J.; Yin, H.; Shi, X.; Yang, R.; Dresselhaus, M. The Nature of Strength Enhancement and Weakening by Pentagon-Heptagon Defects in Graphene. *Nat. Mat.* **2012**, *11*, 759-763.
- 12. Shekhawat, A.; Ritchie, R. O. Toughness and Strength of Nanocrystalline Graphene. *Nat. Comm.* **2016**, *7*, 10546.
- 13. Cervenka, J.; Katsnelson, M. I.; Flipse, C. F. J. Room-Temperature Ferromagnetism in Graphite Driven by Two-Dimensional Networks of Point defects. *Nat. Phys.* **2009**, *5*, 840-844.
- 14. Ni, B.; Zhang, T.; Li, J.; Li, X.; Gao, H. Topological Design of Graphene. In *Handbook of Graphene*, Celasco, E.; Chaika, A. N.; Stauber, T.; Zhang, M.; Ozkan, C.; Ozkan, U.; Palys, B.; Harun, S. W., Eds. Wiley: New York, **2019**.
- 15. Batzill, M. The Surface Science of Graphene: Metal Interfaces, CVD Synthesis, Nanoribbons, Chemical Modifications, and Defects. *Surf. Sci. Rep.* **2012**, *67*, 83-115.
- 16. Wang, R.; Ren, X.-G.; Yan, Z.; Jiang, L.-J.; Sha, W. E. I.; Shan, G.-C. Graphene Based Functional Devices: A Short Review. *Front. Phys.* **2018**, *14*, 13603.
- 17. Cusati, T.; Fiori, G.; Gahoi, A.; Passi, V.; Lemme, M. C.; Fortunelli, A.; Iannaccone, G. Electrical Properties of Graphene-Metal Contacts. *Sci. Rep.* **2017**, *7*, 5109.
- 18. Klein, B. P.; van der Heijden, N. J.; Kachel, S. R.; Franke, M.; Krug, C. K.; Greulich, K. K.; Ruppenthal, L.; Müller, P.; Rosenow, P.; Parhizkar, S., et al. Molecular Topology and the Surface Chemical Bond: Alternant Versus Nonalternant Aromatic Systems as Functional Structural Elements. *Phys. Rev. X* **2019**, *9*, 011030.
- 19. Gottfried, J. M.; Vestergaard, E. K.; Bera, P.; Campbell, C. T. Heat of Adsorption of Naphthalene on Pt(111) Measured by Adsorption Calorimetry. *J. Phys. Chem. B* **2006**, *110*, 17539-17545.
- 20. Mallion, R. B.; Rouvray, D. H. The Golden Jubilee of the Coulson-Rushbrooke Pairing Theorem. *J. Math. Chem.* **1990**, *5*, 1-21.
- 21. Coulson, C. A.; Rushbrooke, G. S. Note on the Method of Molecular Orbitals. *J. Phys.: Condens. Matter* **1940**, *36*, 193-200.
- 22. *CRC Handbook of Chemistry and Physics*; Lide, D. R., Ed.; 90 ed.; CRC Press: Boca Raton, FL, **2010**.

- 23. Xin, H.; Gao, X. Application of Azulene in Constructing Organic Optoelectronic Materials: New Tricks for an Old Dog. *ChemPlusChem* **2017**, *82*, 945-956.
- 24. Koch, N. Organic Electronic Devices and Their Functional Interfaces. *ChemPhysChem* **2007**, *8*, 1438-1455.
- 25. Kahn, A.; Koch, N.; Gao, W. Electronic Structure and Electrical Properties of Interfaces between Metals and  $\pi$ -Conjugated Molecular Films. *J. Polym. Sci. B* **2003**, *41*, 2529-2548.
- 26. *The Molecule-Metal Interface*; Koch, N.; Ueno, N.; Wee, A. T. S., Eds.; Wiley-VCH: Weinheim, **2013**.
- 27. Dahlgren, D.; Hemminger, J. C. Symmetry Extinction of Leed Beams for Naphthalene Adsorbed on Pt(111). *Surf. Sci.* **1981,** *109*, 513-518.
- 28. Dahlgren, D.; Hemminger, J. C. Chemisorption and Thermal Chemistry of Azulene and Naphthalene Adsorbed on Pt(111). *Surf. Sci.* **1982,** *114,* 459-470.
- 29. Dahlgren, D.; Hemminger, J. C. Chemisorption and Ordering of Naphthalene and Azulene on Pt[7(111)×(100)]: The Effect of Periodic Defects on Long Range Order. *Surf. Sci.* **1983**, *134*, 836-848.
- 30. Gland, J. L.; Somorjai, G. A. Low Energy Eelektron Diffraction and Work Function Studies of Benzene, Naphthalene and Pyridine Adsorbed on Pt(111) and Pt(100) Single Crystal Surfaces. *Surf. Sci.* **1973**, *38*, 157-186.
- 31. Hallmark, V. M.; Chiang, S.; Brown, J. K.; Wöll, C. Real-Space Imaging of the Molecular Organization of Naphthalene on Pt(111). *Phys. Rev. Lett.* **1991**, *66*, 48-51.
- 32. Hallmark, V. M.; Chiang, S.; Meinhardt, K.-P.; Hafner, K. Observation and Calculation of Internal Structure in Scanning Tunneling Microscopy Images of Related Molecules. *Phys. Rev. Lett.* **1993**, *70*, 3740-3743.
- 33. Hallmark, V. M.; Chiang, S. Imaging Structural Details in Closely Related Molecular Adsorbate Systems. *Surf. Sci.* **1993**, *286*, 190-200.
- 34. Morin, C.; Simon, D.; Sautet, P. Trends in the Chemisorption of Aromatic Molecules on a Pt(111) Surface: Benzene, Naphthalene, and Anthracene from First Principles Calculations. *J. Phys. Chem. B* **2004**, *108*, 12084 12091.
- 35. Santarossa, G.; Iannuzzi, M.; Vargas, A.; Baiker, A. Adsorption of Naphthalene and Quinoline on Pt, Pd and Rh: A DFT Study. *Chem. Phys. Chem.* **2008**, *9*, 401-413.
- 36. Stuckless, J. T.; Frei, N. A.; Campbell, C. T. A Novel Single-Crystal Adsorption Calorimeter and Additions for Determining Metal Adsorption and Adhesion Energies. *Rev. Sci. Instrum.* **1998**, *69*, 2427-2438.
- 37. Silbaugh, T. L.; Campbell, C. T. Energies of Formation Reactions Measured for Adsorbates on Late Transition Metal Surfaces. *J. Phys. Chem. C* **2016**, *120*, 25161-25172.
- 38. Lytken, O.; Lew, W.; Harris, J. J. W.; Vestergaard, E. K.; Gottfried, J. M.; Campbell, C. T. Energetics of Cyclohexene Adsorption and Reaction on Pt(111) by Low-Temperature Microcalorimetry. *J. Am. Chem. Soc.* **2008**, *130*, 10247-10257.
- 39. Solomonov, B. N.; Varfolomeev, M. A.; Nagrimanov, R. N.; Novikov, V. B.; Zaitsau, D. H.; Verevkin, S. P. Solution Calorimetry as a Complementary Tool for the Determination of Enthalpies of Vaporization and Sublimation of Low Volatile Compounds at 298.15K. *Thermochim. Acta* **2014**, *589*, 164-173.
- 40. Kováts, E.; Günthard, H. H.; Plattner, P. A. Thermische Eigenschaften von Azulenen. *Helv. Chim. Acta* **1955**, *38*, 1912-1919.
- 41. Chickos, J.; Hesse, D.; Hosseini, S.; Nichols, G.; Webb, P. Sublimation Enthalpies at 298.15k Using Correlation Gas Chromatography and Differential Scanning Calorimetry Measurements. *Thermochim. Acta* **1998**, *313*, 101-110.
- 42. Mainka, C.; Bagus, P. S.; Schertel, A.; Strunskus, T.; Grunze, M.; Wöll, C. Linear Dichroism in X-Ray Absorption Spectroscopy of Strongly Chemisorbed Planar Molecules: Role of Adsorption Induced Rehybridisations. *Surf. Sci.* **1995**, *341*, L1055-L1060.
- 43. Doniach, S.; Sunjic, M. Many-Electron Singularity in X-Ray Photoemission and X-Ray Line Spectra from Metals. *J. Phys. C: Solid State Phys.* **1970**, *3*, 285-291.

- 44. Körzdörfer, T.; Kümmel, S. Single-Particle and Quasiparticle Interpretation of Kohn-Sham and Generalized Kohn-Sham Eigenvalues for Hybrid Functionals. *Phys. Rev. B* **2010**, *82*, 155206.
- 45. Kronik, L.; Kümmel, S. Gas-Phase Valence-Electron Photoemission Spectroscopy Using Density Functional Theory. In *First Principles Approaches to Spectroscopic Properties of Complex Materials*, Di Valentin, C.; Botti, S.; Cococcioni, M., Eds. Springer: Berlin, Heidelberg, **2014**; pp 137-191.
- 46. Chong, D. P. Density Functional Theory Study on the Electron Spectra of Naphthalene and Azulene Vapours. *Can. J. Chem.* **2010**, *88*, 787-796.
- 47. Michl, J.; Thulstrup, E. W. Why Is Azulene Blue and Anthracene White? A Simple Mo Picture. *Tetrahedron* **1976**, *32*, 205-209.
- 48. Costa, J. C. S.; Taveira, R. J. S.; Lima, C. F. R. A. C.; Mendes, A.; Santos, L. M. N. B. F. Optical Band Gaps of Organic Semiconductor Materials. *Opt. Mater.* **2016**, *58*, 51-60.
- Vosskötter, S.; Konieczny, P.; Marian, C. M.; Weinkauf, R. Towards an Understanding of the Singlet–Triplet Splittings in Conjugated Hydrocarbons: Azulene Investigated by Anion Photoelectron Spectroscopy and Theoretical Calculations. *Phys. Chem. Chem. Phys.* 2015, 17, 23573-23581.
- 50. Topping, J. On the Mutual Potential Energy of a Plane Network of Doublets. *Proc. R. Soc. Lond. A* **1927**, *114*, 67-72.
- 51. Albano, E. V. A Model for the Work Function Change Caused by Coadsorption. *Appl. Surf. Sci.* **1983**, *14*, 183-193.
- 52. Witte, G.; Lukas, S.; Bagus, P. S.; Wöll, C. Vacuum Level Alignment at Organic/Metal Junctions: "Cushion" Effect and the Interface Dipole. *App. Phys. Lett.* **2005**, *87*, 263502.
- 53. Vázquez, H.; J. Dappe, Y. J.; Ortega, J.; Flores, F. Energy Level Alignment at Metal/Organic Semiconductor Interfaces: "Pillow" Effect, Induced Density of Interface States, and Charge Neutrality Level. *J. Chem. Phys.* **2007**, *126*, 144703.
- 54. Klein, B. P.; Morbec, J. M.; Franke, M.; Greulich, K. K.; Sachs, M.; Parhizkar, S.; Bocquet, F. C.; Schmid, M.; Hall, S. J.; Maurer, R. J., et al. Molecule-Metal Bond of Alternant Versus Nonalternant Aromatic Systems on Coinage Metal Surfaces: Naphthalene Versus Azulene on Ag(111) and Cu(111). *J. Phys. Chem. C* **2019**, *123*, 29219-29230.
- 55. Martínez, J. I.; Merino, P.; Pinardi, A. L.; Gonzalo, O.-I.; López, M. F.; Méndez, J.; Martín-Gago, J. A. Role of the Pinning Points in Epitaxial Graphene Moiré Superstructures on the Pt(111) Surface. *Sci. Rep.* **2016**, *6*, 20354.
- 56. Kruszewski, J.; Krygowski, T. M. Definition of Aromaticity Basing on the Harmonic Oscillator Model. *Tetrahedron Lett.* **1972,** *13*, 3839-3842.
- 57. Roos, P.; Bertel, E.; Rendulic, K. D. Observation of an sp-Derived Surface Resonance on Pt(111) Indicating the Crucial Role of Surface States in Physisorption. *Chem. Phys. Lett.* **1995**, *232*, 537-541.
- 58. Hirshfeld, F. L. Bonded-Atom Fragments for Describing Molecular Charge Densities. *Theor. Chim. Acta* **1977**, *44*, 129-138.
- 59. Bultinck, P.; Van Alsenoy, C.; Ayers, P. W.; Carbó-Dorca, R. Critical Analysis and Extension of the Hirshfeld Atoms in Molecules. *J. Chem. Phys.* **2007**, *126*, 144111.
- 60. Vanpoucke, D. E. P.; Bultinck, P.; Van Driessche, I. Extending Hirshfeld-I to Bulk and Periodic Materials. *J. Comput. Chem.* **2013**, *34*, 405-417.
- 61. Vanpoucke, D. E. P.; Van Driessche, I.; Bultinck, P. Reply to 'Comment on "Extending Hirshfeld-I to Bulk and Periodic Materials". *J. Comput. Chem.* **2013**, *34*, 422-427.
- 62. Bader, R. F. W. *Atoms in Molecules a Quantum Theory*. Oxford University Press: Oxford, **1990**.
- 63. Maurer, R. J.; Ruiz, V. G.; Tkatchenko, A. Many-Body Dispersion Effects in the Binding of Adsorbates on Metal Surfaces. *J. Chem. Phys.* **2015**, *143*, 102808.
- Maurer, R. J.; Ruiz, V. G.; Camarillo-Cisneros, J.; Liu, W.; Ferri, N.; Reuter, K.; Tkatchenko,
   A. Adsorption Structures and Energetics of Molecules on Metal Surfaces: Bridging
   Experiment and Theory. *Prog. Surf. Sci.* 2016, 91, 72-100.

- 65. Maurer, R. J.; Liu, W.; Poltavsky, I.; Stecher, T.; Oberhofer, H.; Reuter, K.; Tkatchenko, A. Thermal and Electronic Fluctuations of Flexible Adsorbed Molecules: Azobenzene on Ag(111). *Phys. Rev. Lett.* **2016**, *116*, 146101.
- 66. Raupach, M.; Tonner, R. A Periodic Energy Decomposition Analysis Method for the Investigation of Chemical Bonding in Extended Systems. *J. Chem. Phys.* **2015**, *142*, 194105.
- 67. Pecher, L.; Tonner, R. Deriving Bonding Concepts for Molecules, Surfaces, and Solids with Energy Decomposition Analysis for Extended Systems. *WIREs Comput Mol Sci.* **2019**, *9*, e1401.
- 68. Mitoraj, M. P.; Michalak, A.; Ziegler, T. A Combined Charge and Energy Decomposition Scheme for Bond Analysis. *J. Chem. Theory Comput.* **2009**, *5*, 962-975.
- 69. Mingos, D. M. P. A Historical Perspective on Dewar's Landmark Contribution to Organometallic Chemistry. *J. Organomet. Chem.* **2001**, *635*, 1-8.
- 70. Ajo, H. M.; Ihm, H.; Moilanen, D. E.; Campbell, C. T. Calorimeter for Adsorption Energies of Larger Molecules on Single Crystal Surfaces. *Rev. Sci. Instrum.* **2004**, *75*, 4471-4480.
- 71. Lew, W.; Lytken, O.; Farmer, J. A.; Crowe, M. C.; Campbell, C. T. Improved Pyroelectric Detectors for Single Crystal Adsorption Calorimetry from 100 to 350 K. *Rev. Sci. Instrum.* **2010**, *81*, 024102.
- 72. King, D. A.; Wells, M. G. Molecular Beam Investigation of Adsorption Kinetics on Bulk Metal Targets: Nitrogen on Tungsten. *Surf. Sci.* **1972**, *29*, 454-482.
- 73. Kresse, G.; Hafner, J. Ab Initio Molecular Dynamics for Liquid Metals. *Phys. Rev. B* **1993**, 47, 558-561.
- 74. Kresse, G.; Hafner, J. Ab Initio Molecular-Dynamics Simulation of the Liquid-Metal-Amorphous-Semiconductor Transition in Germanium. *Phys. Rev. B* **1994**, *49*, 14251-14269.
- 75. Kresse, G.; Furthmüller, J. Efficient Iterative Schemes for Ab Initio Total-Energy Calculations Using a Plane-Wave Basis Set. *Phys. Rev. B* **1996**, *54*, 11169-11186.
- 76. Kresse, G.; Furthmüller, J. Efficiency of Ab-Initio Total Energy Calculations for Metals and Semiconductors Using a Plane-Wave Basis Set. *Comput. Mat. Sci.* **1996**, *6*, 15-50.
- 77. Perdew, J. P.; Burke, K.; Ernzerhof, M. Generalized Gradient Approximation Made Simple. *Phys. Rev. Lett.* **1996**, *77*, 3865-3868.
- 78. Grimme, S.; Antony, J.; Ehrlich, S.; Krieg, H. A Consistent and Accurate Ab Initio Parametrization of Density Functional Dispersion Correction (DFT-D) for the 94 Elements H-Pu. *J. Chem. Phys.* **2010**, *132*, 154104.
- 79. Becke, A. D.; Johnson, E. R. A Density-Functional Model of the Dispersion Interaction. *J. Chem. Phys.* **2005**, *123*, 154101.
- 80. Blöchl, P. E. Projector Augmented-Wave Method. Phys. Rev. B 1994, 50, 17953-17979.
- 81. Kresse, G.; Joubert, D. From Ultrasoft Pseudopotentials to the Projector Augmented-Wave Method. *Phys. Rev. B* **1999**, *59*, 1758-1775.
- 82. Clark, S. J.; Segall, M. D.; Pickard, C. J.; Hasnip, P. J.; Probert, M. I. J.; Refson, K.; Payne, M. C. First Principles Methods Using CASTEP. *Z. Kristallogr. Cryst. Mater.* **2009**, *220*, 567–570.
- 83. Mizoguchi, T.; Tanaka, I.; Gao, S.-P.; Pickard, C. J. First-Principles Calculation of Spectral Features, Chemical Shift and Absolute Threshold of ELNES and XANES Using a Plane Wave Pseudopotential Method. *J. Phys.: Condens. Matter* **2009**, *21*, 104204.
- 84. Triguero, L.; Pettersson, L. G. M.; Ågren, H. Calculations of Near-Edge X-Ray-Absorption Spectra of Gas-Phase and Chemisorbed Molecules by Means of Density-Functional and Transition-Potential Theory. *Phys. Rev. B* **1998**, *58*, 8097-8110.
- 85. Klues, M.; Hermann, K.; Witte, G. Analysis of the Near-Edge X-Ray-Absorption Fine-Structure of Anthracene: A Combined Theoretical and Experimental Study. *J. Chem. Phys.* **2014**, *140*, 014302.
- 86. Diller, K.; Maurer, R. J.; Müller, M.; Reuter, K. Interpretation of X-Ray Absorption Spectroscopy in the Presence of Surface Hybridization. *J. Chem. Phys.* **2017**, *146*, 214701.
- 87. Maurer, R. J.; Reuter, K. Excited-State Potential-Energy Surfaces of Metal-Adsorbed Organic Molecules from Linear Expansion Δ-Self-Consistent Field Density-Functional Theory (ΔSCF-DFT). *J. Chem. Phys.* **2013**, *139*, 014708.

- 88. Becke, A. D.; Johnson, E. R. Exchange-Hole Dipole Moment and the Dispersion Interaction. *J. Chem. Phys.* **2005**, *122*, 154104.
- 89. van Lenthe, E.; Baerends, E. J. Optimized Slater-Type Basis Sets for the Elements 1-118. *J. Comput. Chem.* **2003**, *24*, 1142-1156.
- 90. van Lenthe, E.; Baerends, E. J.; Snijders, J. G. Relativistic Regular Two-Component Hamiltonians. *J. Chem. Phys.* **1993**, *99*, 4597-4610.
- 91. Philipsen, P. H. T.; Baerends, E. J. Relativistic Calculations to Assess the Ability of the Generalized Gradient Approximation to Reproduce Trends in Cohesive Properties of Solids. *Phys. Rev. B* **2000**, *61*, 1773-1778.
- 92. Band 2018, Scm, Theoretical Chemistry, Vrije Universiteit, Amsterdam, the Netherlands, http://www.scm.com.
- 93. te Velde, G.; Baerends, E. J. Precise Density-Functional Method for Periodic Structure. *Phys. Rev. B* **1991**, *44*, 7888.

# **TOC GRAPHIC**

# **SUPPORTING INFORMATION**

# for

# Enhanced Bonding of Pentagon-Heptagon Defects in Graphene to Metal Surfaces: Insights from the Adsorption of Azulene and Naphthalene to Pt(111)

Benedikt P. Klein<sup>a</sup>, S. Elizabeth Harman<sup>b</sup>, Lukas Ruppenthal<sup>a</sup>, Griffin M. Ruehl<sup>b</sup>, Samuel J. Hall<sup>c,d</sup>, Spencer J. Carey<sup>b</sup>, Jan Herritsch<sup>a</sup>, Martin Schmid<sup>a</sup>, Reinhard J. Maurer<sup>d</sup>, Ralf Tonner<sup>a</sup>, Charles T. Campbell<sup>b</sup>, J. Michael Gottfried<sup>a</sup>

<sup>a</sup>Fachbereich Chemie, Philipps-Universität Marburg, Hans-Meerwein-Straße. 4, 35032 Marburg, Germany

<sup>b</sup>Department of Chemistry, University of Washington, Bagley Hall, Seattle, WA 98195, United States of America

<sup>c</sup>MAS Centre for Doctoral Training, Senate House, and <sup>d</sup>Department of Chemistry and Centre for Scientific Computing, University of Warwick, Gibbet Hill Road, Coventry, CV4 7AL, United Kingdom

#### I. Treatment of the NEXAFS Data

The NEXAFS data acquired at the HE-SGM beamline in BESSY was treated in the following way to obtain the NEXAFS spectra shown in the main text. All spectra were calibrated of the photon energy by means of the carbon-related absorption on the gold grid. The spectra were then normalized in the pre-edge region at 282 eV. For background correction, the spectra of the clean Pt(111) substrate were fitted and then subtracted from the sample spectra. Finally, the sample spectra were normalized to the absorption edge at 310 eV.

# II. XPS Multilayer Spectra

Figure S1 shows the multilayer spectra of azulene and naphthalene on Pt(111). The asymmetry visible in the monolayer spectra (Figure 4 of the main text) is not present here.

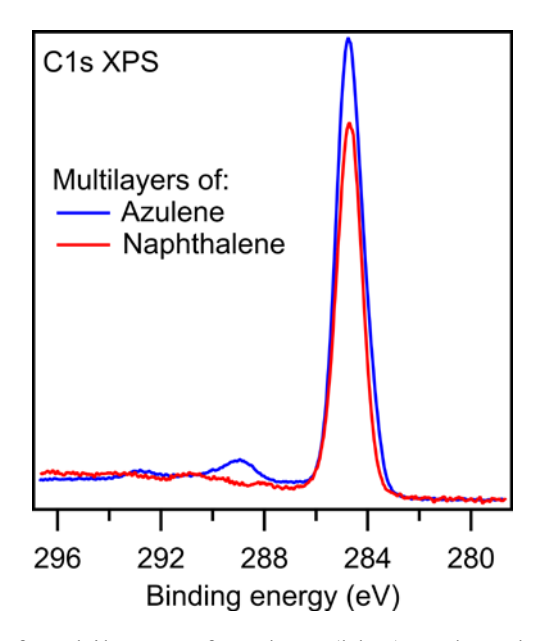


**Figure S1.** XP spectra of multilayers of azulene (blue) and naphthalene (red), taken with monochromatic Al  $K_{\alpha}$  radiation. The asymmetry exhibited by the monolayer peaks is absent in the multilayer. The shoulder of the azulene peak at lower binding energies can be attributed to the chemically different carbon atoms.<sup>1</sup>

# **III. DFT Orbital Energies**

The modified Kohn-Sham (KS) orbital energies displayed in Figure 4b of the main text were obtained by stretching the raw PBE KS-orbital energies by a factor of 1.2 and converting them to the binding energy scale of the experiment (positive binding energies relative to  $E_F$ ) by adding a shift of 3.45 eV. This procedure was already reported for the simulation of UP spectra of similar molecules.<sup>2-3</sup>

**Table S1.** Orbital energies for occupied Kohn-Sham orbitals of the gas phase-optimized structures for azulene and naphthalene as obtained by DFT (PBE/def2-TZVPP), as well as the orbital energies after stretching and shifting to the experimental energy scale (positive binding energies relative to  $E_{\rm F}$ ), all energies in eV

	naphthalene			azulene	
orbital	PBE	mod-PBE	orbital	PBE	mod-PBE
1a <sub>u</sub>	-5.48	3.13	$2a_2$	-4.93	2.47
2b3 <sub>u</sub>	-6.14	3.92	$3b_1$	-5.94	3.68
$1b_{2g}$	-7.17	5.15	$1a_2$	-7.50	5.55
$9a_g$	-7.91	6.04	$17a_1$	-7.95	6.09
$1b_{1g}$	-8.08	6.25	$2b_1$	-8.21	6.41
$6b_{3g}$	-8.10	6.27	$12b_2$	-8.56	6.82
$7b_{2u}$	-8.84	7.16	16a <sub>1</sub>	-8.97	7.31
$7b_{1u}$	-9.68	8.17	$11b_2$	-9.06	7.43
$1b_{3u}$	-9.69	8.17	15a <sub>1</sub>	-9.49	7.94
$6b_{2u}$	-10.05	8.61	$1b_1$	-9.61	8.09
$5b_{3g}$	-10.12	8.70	$10b_{2}$	-9.86	8.39
$8a_g$	-10.72	9.41	$9b_2$	-10.98	9.72
$6b_{1u}$	-10.89	9.62	$14a_1$	-11.05	9.81
$7a_{\rm g}$	-12.06	11.02	$13a_1$	-12.08	11.04
$4b_{3g}$	-12.45	11.49	$8b_2$	-12.58	11.64
$5b_{2u}$	-12.63	11.70	$12a_1$	-13.42	12.66
$6a_g$	-14.66	14.15	$11a_1$	-13.53	12.79
$5b_{1u}$	-15.07	14.63	$7b_2$	-15.19	14.78
$4b_{2u}$	-15.34	14.96	$10a_1$	-15.94	15.67
$3b_{3g}$	-17.73	17.83	$6b_2$	-17.35	17.37
$5a_g$	-18.23	18.43	9a <sub>1</sub>	-18.21	18.40
$4b_{1u}$	-19.18	19.56	$5b_2$	-19.47	19.91
$3b_{2u}$	-20.30	20.91	$8a_1$	-20.40	21.03
$4a_{\rm g}$	-21.72	22.61	$7a_1$	-21.73	22.62

### IV. Packing of the Azulene and Naphthalene Molecules

The C1s XPS intensity of the saturated monolayer is higher for azulene than for naphthalene, as can be seen in Figure 4 in the main text. We think the higher intensity is not an artefact but that azulene has a slightly higher coverage. The limit of the saturation coverage is the tightest packing of the molecules. To show the different packing behavior of the molecules we calculated the energies for 2D periodic layers of molecules (without the Pt(111) surface) with dispersion corrected periodic DFT at a number of inter-molecular distances. The molecules were placed in a hexagonal lattice, with two molecular orientations (Figures S2a,c and S2b,d). The resulting interaction energy of the molecules as a function of the molecule-molecule distance is plotted in Figure S2e.

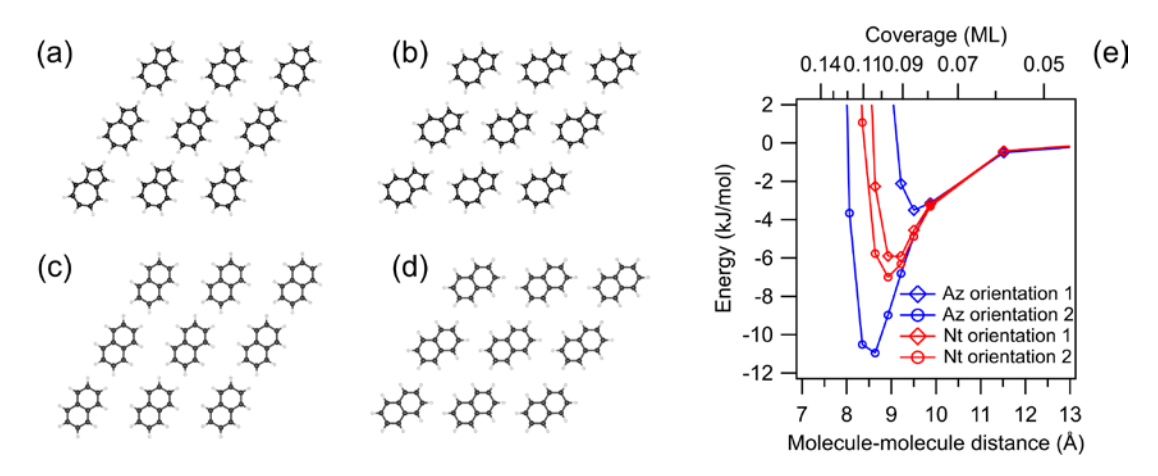


**Figure S2.** Intermolecular interactions: 2D periodic structures used to calculate the molecule-molecule interaction energy of azulene (top) and naphthalene (bottom) (a,c) orientation 1, (b,d) orientation 2. (e) Interaction energy as a function of molecule-molecule distance.

The calculated energies are mostly comprised of van-der-Waals attraction and steric (Pauli) repulsion, as no surface is included and the electrostatic repulsion of the surface dipoles is thus absent. Both molecules experience an attractive potential when the inter-molecular distance is decreased from large distances. At smaller distances the energy has a minimum and finally rises steeply as the molecules get in the range of steric repulsion. Because of the box-like shape of the naphthalene molecule the orientation (Figure S2c,d) is not important for its interaction energy. For azulene, however, orientation 2, where the molecule is rotated by 30° relative to the hexagonal lattice (Figure S2b), yields a more favorable interaction with a deeper minimum and a closer distance for the onset of repulsion (Figure S2e). Thus, the azulene molecules can in principle pack closer and form a structure with higher coverage. If the relative coverages are calculated by the minima of the interaction energy from Fig S2e, the azulene coverage is higher by 7% than the naphthalene coverage, which is within the margin of error of the experimental results. The real coverage on the surface is also influenced by other factors such as the adsorption sites, which the molecules can occupy, but the steric repulsion should not be influenced as the lowest limit of the intermolecular distance.

# V. Details of the Topping Fit Procedure

The data of the work function change was fitted using the Topping model. The Topping model describes the depolarization of the vertical dipoles with increasing coverage.<sup>4-5</sup>

The experimental work function change  $\Delta\Phi$  was fitted with Equation (S1), where  $\mu_0$  is the unattenuated dipole moment per molecule,  $\sigma$  the absolute coverage in molecules per m<sup>2</sup>, and  $\alpha$  the polarizability volume in m<sup>3</sup>, and  $\varepsilon_0$  the electric constant.

$$\Delta \Phi = \frac{\mu_0 \cdot \sigma}{\varepsilon_0} \left( 1 + 9\alpha \cdot \sigma^{3/2} \right)^{-1} \tag{S1}$$

To obtain the unattenuated dipole moment from the DFT calculations, the Topping fit was modified to be applied on the (partly attenuated) dipole moments of the six calculated structures.

The resulting Equation (S2) was used to fit the dipole moment directly.

$$\mu = \mu_0 \cdot (1 + 9\alpha \cdot \sigma^{3/2})^{-1} \tag{S2}$$

# VI. Discussion of Experimental WF Change and Dipole Moments from DFT

Table 1 in the main text only shows the work function change only for the monolayer coverage. In Figure S3 the experimental and theoretical WF changes are compared for all coverages available.

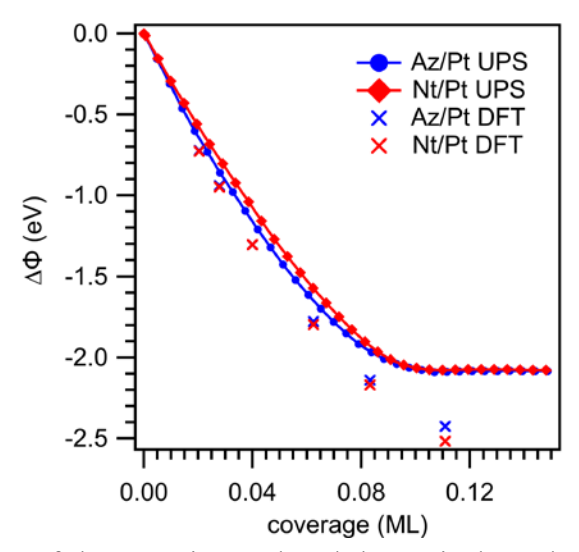


**Figure S3.** Compilation of the experimental and theoretical results for the work function changes at different coverages. Red lines with diamonds, experimental values for naphthalene; blue lines with circles, experimental values for azulene; crosses, theoretical values for azulene (blue) and naphthalene (red).

The DFT results overestimate the WF change for all coverages, the magnitude of the error gets larger with increasing coverage. Both experiment and theory show similar values for azulene and naphthalene over the whole coverage range.

Contributions to the vertical dipole moments: The total vertical dipole moment of the adsorbate comprises the following major contributions: (1) the dipole caused by the adsorption-induced out-of-plane distortion of the molecules, (2) the Pauli-pushback dipole moment, and (3) the charge transfer dipole moment. The charge rearrangement (seen in Figure 7 of the main text) encompasses all three effects and shows the complex overall situation. The three contributions are interdependent and therefore probably not simply additive. In an attempt to quantify the different contributions in an approximate way, we make the following considerations:

Table S2 compares the vertical dipole moments calculated for the adsorbate structures, the surface fragments, the deformed molecular layers in the adsorbate structure, and the deformed isolated molecules. For reference, we added data for the adsorption of the same molecules on Cu(111), on which azulene is chemisorbed —although more weakly than on Pt(111)—, while naphthalene is physisorbed. A detailed description of the bonding

situation on Cu(111) was recently published.<sup>1</sup> All dipole moments were calculated in ADF BAND with the same parameters used for the pEDA calculations (see section XII).

In all systems, the separate surface fragments do not show any appreciable dipole moment. In systems without charge transfer or deformation, such as naphthalene on Cu(111), the adsorbate still induces a substantial dipole moment, which is attributed to the Paulipushback effect. In the more strongly interacting systems, the molecules undergo out-of-plane deformation and thus develop dipole moments, as can be seen by the values for the deformed molecular layers and the isolated deformed molecules. The dipole moments of the deformed molecules are somewhat reduced in the periodic structure, because of the mutual depolarization between neighboring dipoles. The total dipole moment of the adsorbate structure is larger than the dipole moment of the deformed molecules by a factor of approximately 2, from which one may conclude that the deformation is responsible for about half of the dipole moment of the adsorbate structure. However, the different contributions are probably not additive, because the molecular electronic structure is strongly affected by the interaction with the surface. As a result, the dipole moment of the adsorbed molecule will be different from that of the deformed isolated molecule.

An alternative, indirect way to estimate the deformation-related contributions to the dipole moment is to calculate the vertical dipole moment of the undeformed adsorbed molecule. The vertical dipole moment of the undeformed azulene and naphthalene molecules adsorbed on the Pt(111) surface (with the same adsorption height for the center of mass as in the fully relaxed structure) is also given in Table S2. This approach indicates that about 1.2 D or 25 % of the vertical dipole moment is caused by the deformation of the molecule.

**Table S2.** Comparison of the vertical dipole moments of surface fragments, deformed molecular layer in the same unit cell, deformed molecule isolated without any periodicity, the undeformed adsorbed molecule, and the relaxed adsorbate structures for azulene (Az) and naphthalene (Nt) on Pt(111) and Cu(111).

Dipole moment (in D) of:	Az/Pt(111)	Nt/Pt(111)	Az/Cu(111)	Nt/Cu(111)
Surface (fragment)	-0.04	-0.04	0.01	0.00
Deformed molecular layer	2.27	2.15	0.71	-0.06
Isolated deformed molecule	2.66	2.53	0.92	-0.07
Undeformed adsorbed molecule	3.62	3.60	-	-
Relaxed adsorbate structure	4.77	4.79	2.41	1.90

# VII. Coverage Dependence of the Adsorption Heights

The adsorption heights obtained the DFT-D3 optimized structures depend on the reference value used for their calculation. If the average height of the first platinum layer in the adsorbate structure is chosen as a reference, a false trend is visible with the largest adsorption height for the smallest coverage (Triangles, Figure S4). This false trend is caused by the deformation of the surface underneath the molecules, reducing the adsorption height significantly for the higher coverages. The trend is not present, if either only the seven Pt-atoms directly beneath the molecule, or the height of the relaxed surface without molecule is chosen as reference. The adsorption heights calculated using only the atoms beneath the molecule are closer to the local bond length between carbon and platinum atoms but are less comparable to values for molecules with a different adsorption site. Thus the heights are best calculated as the average height of all carbon atoms above the average height of the first layer of the relaxed, clean Pt(111) surface (Table S3).

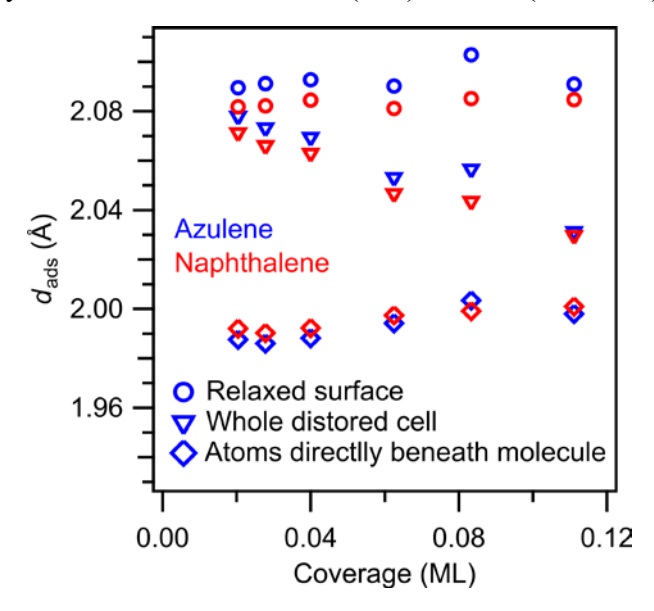


**Figure S4**: adsorption height calculated with three reference systems: The relaxed surface height without molecules (circles), the whole first layer in the unit cell (triangles) and the seven atoms directly beneath the molecule (diamonds).

**Table S3.** Adsorption heights of azulene and naphthalene on Pt(111) calculated for the six different coverages. The adsorption height are given relative to the relaxed surface.

supercell	coverage / ML	adsorption	height / Å
		Az/Pt	Nt/Pt
3×3	0.111	2.091	2.085
$(2\sqrt{3} \times 2\sqrt{3})R30^{\circ}$	0.083	2.103	2.085
4×4	0.063	2.090	2.081
5×5	0.040	2.093	2.084
6×6	0.028	2.091	2.082
7×7	0.020	2.090	2.082

# VIII. Discussion of the Adsorbate Structure

The carbon backbones of the molecules are distorted by the adsorption, with naphthalene showing a symmetric deformation with the bridging atoms closest to the surface and a reduced butterfly angle (defined as the angle of fold between the two aromatic rings, 180° in the free molecule) of 171°. The azulene molecule exhibits a smaller butterfly distortion (175°) but is overall slightly tilted with the five-membered ring closer to the surface.

Upon adsorption, most C-C bonds in the molecules become elongated (between 1.2 and 7.9 pm for naphthalene and between 1.3 and 9.2 pm for azulene) as would be expected for the transition from aromatic bonds between  $\rm sp^2$  carbons towards single bonds between  $\rm sp^3$  carbons (Fig 6e,f). The single exception is the bridging bond in the azulene molecule, which gets shorter by -4.1 pm upon adsorption, indicating an increased double-bond character. The unusual shortening of this bridging bond can be explained by the donation of charge into the former LUMO of the molecule, which is  $\pi$ -bonding with respect to the bridging bond as discussed for adsorption on Cu(111) before.<sup>1</sup>

Another indication for the loss of aromaticity is the out of plane deformation of the molecules. The C-H bonds of both molecules are strongly tilted away from the surface, indicating rehybridization of the formerly planar  $sp^2$  carbon atoms towards the tetrahedral  $sp^3$  state (Figure 6c,d). In naphthalene, the four  $\alpha$ -positioned hydrogen atoms show a larger out-of-plane angle (38°) than those at the  $\beta$ -positions (17°), whereas the hydrogen atoms in azulene are more displaced in the five-membered ring (40°) than in the seven-membered ring (17°). If one assumes a complete rehybridization to  $sp^3$  with the surface as fourth bonded neighbor (perpendicular to the angular plane) the situation is similar as in the Platonic hydrocarbon cubane. In this molecule, the out-of-plane angle of the C-H bonds is 35°, which is close to the calculated values in our systems.

All of the discussed structural parameters show a more complex distortion of the azulene molecule and the surface beneath. This difference between azulene and naphthalene is partly due to the lower symmetry of azulene, but also the expression of a more complex surface chemical bond characterized by a partially localized interaction between atoms in the molecule and of the surface, which is more pronounced for azulene than for naphthalene as discussed below.

# IX. Dependence of the DFT-calculated Adsorption Energies on the Adsorption Site

To test the dependence of the DFT-calculated adsorption energy on the adsorption site, we started structural optimizations from several different starting geometries. The adsorption energy decreases with coverage for the same adsorption site for both molecules as expected due to intermolecular repulsion. Azulene is stronger bonded throughout all adsorption sites and coverages.

**Table S4.** Adsorption energies  $E_{ads}$  of azulene and naphthalene on Pt(111) calculated for several adsorption sites and three different coverages. All energies in (kJ/mol).<sup>1</sup>

		Az/Pt	Az/Pt		Nt/Pt	
supercell	coverage	adsorption site	$E_{ m ads}$	adsorption site	$E_{ m ads}$	
3×3	0.111	on-top fcc-hcp 5°	-306	on-top fcc-hcp 30°	-181	
		on-top hep-fee 5°	-310	-	-	
		on-top hcp-fcc-10°	-308	on-top 0°	-258	
		bridge hcp-hcp 0°	-260	bridge hcp-hcp 0°	-214	
		bridge hcp-hcp 15°	-275	bridge hcp-hcp 10°	-210	
$(2\sqrt{3} \times 2\sqrt{3})-$ R30°	0.083	on-top fcc-hcp 15°	-340	on-top fcc-hcp 30°	-212	
		on-top hcp-fcc 15°	-340	-	-	
		on-top hcp-fcc-10°	-335	on-top 0°	-298	
		bridge hcp-hcp 0°	-304	bridge hcp-hcp 0°	-264	
4×4		on-top fcc-hcp 15°	-362	on-top fcc-hcp 30°	-233	
	0.063	on-top hcp-fcc 15°	-361	-	-	
		on-top hcp-fcc 10°	-361	on-top 0°	-317	
		bridge hcp-hcp 15°	-327	bridge hcp-hcp 0°	-283	
		bridge fcc-fcc 0°	-317	-	-	

<sup>1</sup>The obtained relaxed adsorption structures and the different sites are named using a three-component scheme according to the relative orientations of the molecule and the surface lattice. The first part of the name denotes the position of the central point of the bridging C-C bond relative to the surface: directly above of a Pt-atom ("on-top") or directly above the shortest connection of two Pt-atoms ("bridge"). The second part denotes (where applicable to the respective structure) whether the molecular rings are positioned over a fcc or a hcp site (for azulene, the first value refers to the 5-membered ring and the second to the 7-membered ring). The last parameter describes the angle between the long axis of the molecule (perpendicular to the bridging bond) and the [110] direction of the surface.

## X. HOMA Analysis

A widely used approach to quantify aromaticity is the harmonic oscillator model of aromaticity (HOMA)<sup>7</sup>, which is based on the molecular geometry and takes the deviation of the bond lengths from the ideal aromatic bond into account.

The HOMA value is calculated as

$$HOMA = 1 - \frac{\alpha}{NB} \sum (R_{opt} - R_i)^2$$
 (S3)

Where NB is the number of bonds and  $R_i$  is each individual bond length. The model parameters  $R_{\rm opt}$  (the optimal C-C bond length of the reference molecule) and  $\alpha$  are chosen such that the benzene molecule (with six equally long bonds) has a HOMA value of 1, whereas the hypothetical Kekulé-like benzene (with three single and three double bonds) has a HOMA value of 0. For the HOMA values discussed below, we used the bond lengths obtained from the DFT-optimized structures, the parameters used to calculate the HOMA values stem from free benzene optimized with the same method ( $R_{\rm opt} = 1.398$  Å and  $\alpha = 362.1$  Å<sup>-2</sup>).

For molecules with more than one ring, different HOMA values can be calculated, depending on which  $\pi$ -bonds and conjugation paths are taken into account. One possibility is to use all  $\pi$ -bonds in the molecule; this is denoted as overall HOMA value O. If only the perimeter  $\pi$ -bonds of the molecule are used, this is called the perimeter HOMA value P. In addition, the HOMA value R for each ring can be calculated separately. For convenience, we introduce here the parameter Excess Perimeter Conjugation (EPC), which is defined as EPC = P - O. This parameter provides a simple measure for the degree to which the molecule shows benzenoid or annulenoid aromaticity within in the HOMA concept. A high EPC value indicates predominant annulenoid aromaticity, which means that the aromatic conjugation occurs mainly along the perimeter of the molecule. In contrast, a low EPC value means that conjugation is distributed over the whole molecule equally.

The HOMA value can also be established by an equivalent formalism.<sup>9</sup>

$$HOMA = 1 - \alpha \left[ \left( R_{opt} - R_{av} \right)^2 + \frac{1}{NB} \sum \left( R_{opt} - R_i \right)^2 \right]$$
 (S4)

The first term in the parentheses is the (squared) deviation of the the average bond length in the investigated molecule  $R_{\rm av}$  and the optimal  $R_{\rm opt}$  aromatic bond length and is called EN.

$$EN = \alpha \left( R_{\text{opt}} - R_{av} \right)^2 \tag{S5}$$

*EN* describes the average lengthening or shortening of the bonds in the molecule and is therefore useful to discuss the electron donation in anti-bonding orbitals.

Figure S5 illustrates the HOMA analysis for azulene, naphthalene and the reference molecule benzene both in their gas phase structure and when adsorbed on Pt(111). All structures are optimized DFT geometries.

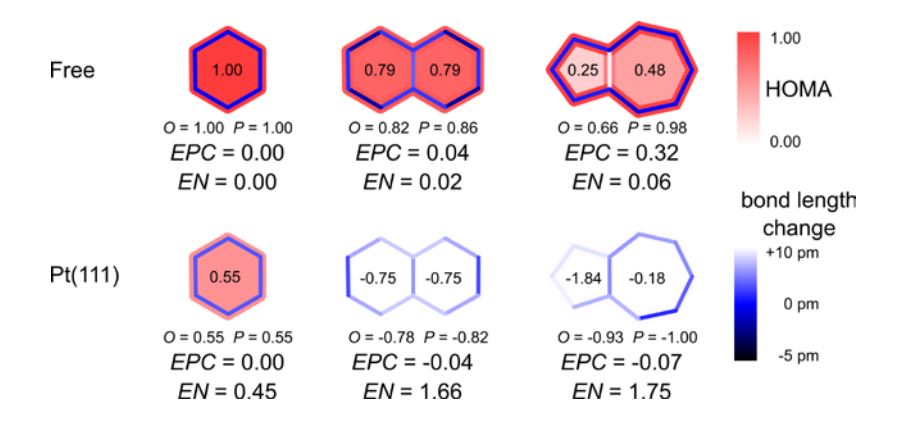


**Figure S5.** (a) HOMA analysis for azulene, naphthalene, and benzene (reference) in the gas phase and adsorbed on Pt(111), based on the DFT optimized structures. The red color scheme shows the HOMA value. The filling of each ring is colored in its respective ring HOMA value (*R*), the perimeter bonds are colored according to the perimeter HOMA value (*P*), and the bridging bonds are colored according to the overall HOMA value (*O*). All bonds are additionally colored with a blue color scheme representing the bond length change with respect to the ideal aromatic bond. For the meaning of *EPC* and *EN*, see the text.

As already indicated by the mesomeric resonance structures, the free azulene molecule shows a high EPC value of 32 and can therefore be regarded as a bridged [10]annulene with electron delocalization mainly around the circumference (*i.e.*, as a cyclodecapentaene with a transannular single-bond bridge). As expected, naphthalene with EPC = 4 is best described as a fully delocalized benzenoid aromatic molecule with a bridging bond of partial double-bond character. When adsorbed on less reactive metals like Ag(111) and Cu(111), azulene shows already a change towards benzenoid character with a lower EPC value and less difference in the bond lengths. On Pt(111), the HOMA analysis reaches its limits. Both for azulene and naphthalene, all bonds are massively elongated as expressed in the large EN values (see Figure S5), leading to negative HOMA values. The donation of electron density in the antibonding orbitals of the molecules thus changes the  $\pi$ -system to an extent that the differences in aromaticity are no longer visible.

## **XI. Charge Partitioning Schemes**

The charge transfer between surface and molecule was quantified using four different methods. These are Hirshfeld charge analysis,  $^{11}$  the iterative Hirshfeld charge analysis,  $^{12}$   $^{14}$  Bader's Atoms in Molecules (AIM) charge analysis,  $^{15}$  and the integration of the molecular DOS up to  $E_F$ . As discussed in the main text, the absolute values vary by quite a large margin. Further analysis using the periodic energy decomposition analysis (pEDA) shows that the charge transfer is governed by a complicated mechanism of donation and back-donation.

**Table S5.** Charge transfer between molecule and surface calculated by different charge partitioning schemes. All charges in units of the elementary charge e, a negative value means charge transfer from the surface to the molecule.

	Az/Pt	Nt/Pt
q(AIM)	+0.02	+0.03
q(Hirshfeld) BAND	-0.35	-0.35
q(Hirshfeld) VASP	-0.21	-0.20
q(Hirshfeld-I) VASP	-0.84	-0.86
q(DOS)	-1.60	-1.70

# XII. Discussion of the pEDA Analysis

The following section contains a more detailed discussion of the periodic energy decomposition analysis, which was discussed briefly in the main text. Table S6 summarizes the results of the pEDA for azulene and naphthalene on Pt(111).

**Table S6.** pEDA results for azulene and naphthalene on Pt(111), all energies are in kJ/mol.

	Az/Pt	Nt/Pt
$\Delta E_{ m int}$	-679	-620
$\Delta E_{\rm int} ({\rm disp})^{\rm a}$	-202 (30 %)	-203 (33 %)
$\Delta E_{\rm int} ({\rm elec})^{\rm a}$	-476 (70 %)	-417 (67 %)
$\Delta E_{ m Pauli}$	+5896	+5971
$\Delta E_{ m elstat}^{ m \ \ b}$	-3430 (54 %)	-3474 (54 %)
$\Delta E_{ m orb}{}^{ m b}$	-2943 (46 %)	-2915 (46 %)
$\Delta E_{\rm orb}({\rm surf}{ ightarrow}{ m mol})^{\rm c}$	-1178 (70 %)	-873 (65 %)
$\Delta E_{\rm orb}({\rm mol}{\rightarrow}{\rm surf})^{\rm c}$	-508 (30 %)	-478 (35 %)
$\Delta E_{\rm prep}$ (mol,in cell) <sup>d</sup>	+283	+279
$\Delta E_{\text{prep}}(\text{mol,free})^{\text{e}}$	+286	+282
$\Delta E_{prep}(surf)$	+58	+38
$\Delta E_{\mathrm{bond}}$	-338	-302
$\Delta E_{\rm bond}$ (PAW)	-335	-298

Percentage values give the relative contributions:

In the following discussion of the values from Table S6, the first energy value is always referring to azulene and the second to naphthalene. For both molecules, the contribution from dispersion attraction is almost identical ( $\Delta E_{\rm int}$  (disp) = -202 and -203 kJ/mol), and makes up about one third of the total interaction energy  $\Delta E_{\rm int}$ .

<sup>&</sup>lt;sup>a</sup> of electronic and dispersion effects to  $\Delta E_{\rm int}$ 

 $<sup>^{\</sup>rm b}$  to the sum of the attractive pEDA terms  $\Delta E_{\rm elstat}$  and  $\Delta E_{\rm orb}$ 

<sup>&</sup>lt;sup>c</sup> to the assignable parts of the orbital terms  $\Delta E_{\rm orb}({\rm surf} \rightarrow {\rm mol})$  and  $\Delta E_{\rm orb}({\rm mol} \rightarrow {\rm surf})$ 

<sup>&</sup>lt;sup>d</sup> referenced to the molecular fragment in the unit cell of the adsorbate structure

<sup>&</sup>lt;sup>e</sup> referenced to the isolated molecular fragment

The preparation energies  $\Delta E_{\text{prep}}$  of molecules and surfaces are also similar but slightly larger for azulene ( $\Delta E_{\text{prep}} = +283$  and +279 kJ/mol), in agreement with its stronger structural deformation visible in Figure 6 of the main text. The most apparent difference between the bonding of azulene and naphthalene to the Pt-surface is in the electronic interaction energies  $\Delta E_{\text{int}}$  (elec) and its constituent parts. The electronic interaction energy is larger by 59 kJ/mol for azulene ( $\Delta E_{\text{int}}$  (elec) = -476 and -417 kJ/mol) translating into the same difference of the total interaction energies of 59 kJ/mol ( $\Delta E_{\text{int}} = -679$  and -620 kJ/mol). Naphthalene shows a larger electrostatic contribution ( $\Delta E_{\text{elstat}} = -3430$  and -3474 kJ/mol), which is then overcompensated by a larger Pauli repulsion term ( $\Delta E_{\text{Pauli}} = +5896$  vs. +5971 kJ/mol), whereas the orbital term is larger for azulene ( $\Delta E_{\text{orb}} = -2943$  vs. -2915 kJ/mol). All three terms indicate a stronger hybridization and a higher proportion of covalent bonding for azulene.

While the differences between azulene and naphthalene in constituent parts of the interaction energy are small compared to the total magnitude of the terms (their proportion is only about 1 %), they are still significant. The large attractive and repulsive terms mostly cancel each other and the small (but significant) difference prevails in the total interaction and bond energies (where the difference is about 10 %).

The pEDA method enables us to look even deeper into the chemical bonding mechanism. Using the natural orbitals for chemical valence (NOCV) extension for the pEDA we can further decompose the orbital interaction term  $\Delta E_{\rm orb}$  and obtain the deformation densities  $\Delta \rho_{\rm i}.^{16\text{-}17}$  As one fragment is a metal surface, the situation is more complex than for molecular systems and many NOCVs contribute to the orbital interaction. However, the principal interactions determining the bonding situation can be identified by a few dominant contributions. Analysis of the deformation densities shows that there are significant contributions stemming both from surface-to-molecule and molecule-to-surface flows of electron density. Figure 10 of the main text shows selected deformation densities for both charge transfer channels for azulene, while and Figures S6 and S7 show the ten deformation densities with the largest eigenvalues.

For each adsorbate system, several of the deformation densities with the largest eigenvalues can be clearly classified and are subjected to further analysis. The deformation densities with smaller eigenvalues cannot unambiguously be assigned to specific interactions. See Tables S7 and S8 for more information and for the classification of all deformation densities.

If the energy contributions of the assignable deformation densities are summed up, they make up 1686 kJ/mol for azulene and 1351 kJ/mol for naphthalene, showing that a higher percentage of the total orbital energy term (57 % vs. 46 %) can be attributed to the main interaction channels for azulene. The energy contributions of the deformation densities can also be summed up depending on whether the deformation densities show electron transfer from the surface to the molecule  $\Delta E_{\rm orb}({\rm surf} \rightarrow {\rm mol})$  or reverse  $\Delta E_{\rm orb}({\rm mol} \rightarrow {\rm surf})$ . For both molecules the surface-to-molecule charge transfer  $\Delta E_{\rm orb}({\rm surf} \rightarrow {\rm mol})$  is the dominating part of the orbital energy (70 % for azulene, 65 % for naphthalene).

The pEDA shows that the bond between the molecules and the surface encompasses massive surface-to-molecule and molecule-to-surface charge transfer contributions. Overall, the various contribution to the total charge transfer almost cancel out, leading to the relatively small charge values resulting from the charge partitioning analysis. In terms of energy, the surface-to-molecule charge transfer has a larger contribution than the reverse charge transfer. The orbital energy term can be pinned as the main cause for the different adsorption energies of azulene and naphthalene, with azulene showing a significantly higher contribution of the dominant orbital interaction to this term.

Tables S7 and S8 show information about the 10 NOCV deformation densities with the largest eigenvalue for both azulene and naphthalene. Figures S6 and S7 show images of all these deformation densities. Seven of these for azulene and six for naphthalene could be classified according to the bonding mechanism they depict. The deformation densities highlighted in blue in Tables S7 and S8 could be identified as showing electron transfer from the molecule to the surface, whereas those highlighted in red show electron transfer from the surface to the molecule. Summation over the corresponding orbital energy terms yields a contribution of about 70% by the surface-to-molecule charge transfer as discussed in the main text and above.

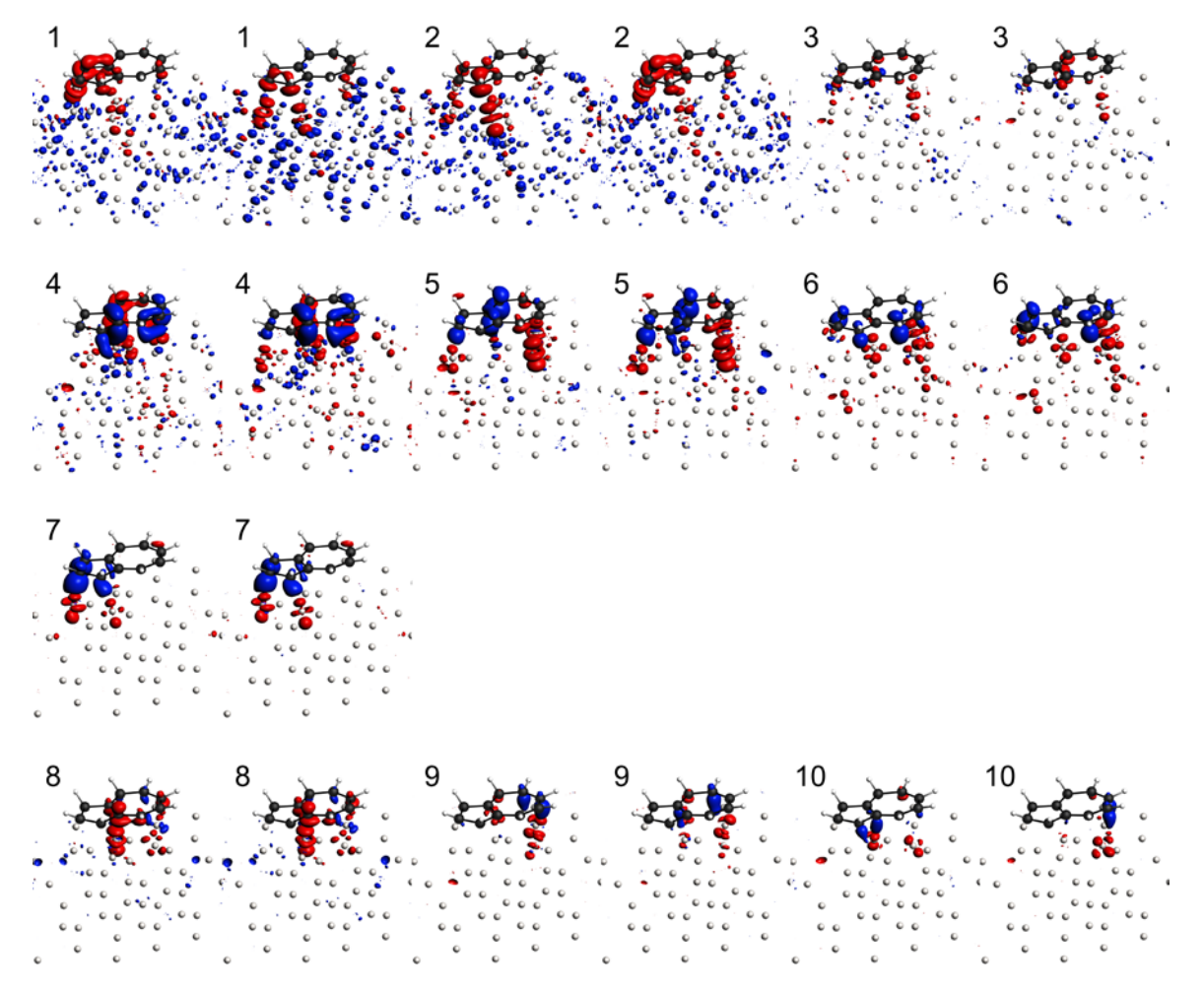


**Figure S6.** NOCV deformation densities  $\Delta \rho_i$  with the largest eigenvalues pEDA plus NOCV analysis for azulene on Pt(111). Red, electron depletion; blue, electron accumulation. The number correspond to the numbers in Table S7, left image Spin 1, right image Spin 2. Isosurface values: 0.003 e<sup>-</sup>/Å<sup>3</sup> for 1 to 3, 0.001 e<sup>-</sup>/Å<sup>3</sup> for 4 to 8, and 0.0005 e<sup>-</sup>/Å<sup>3</sup> for 9 and 10. Deformation densities 1 to 3 show electron transfer from the molecule (and sometimes some of the uppermost surface atoms) to the substrate and 4 to 7 show electron transfer from the substrate to the molecule.

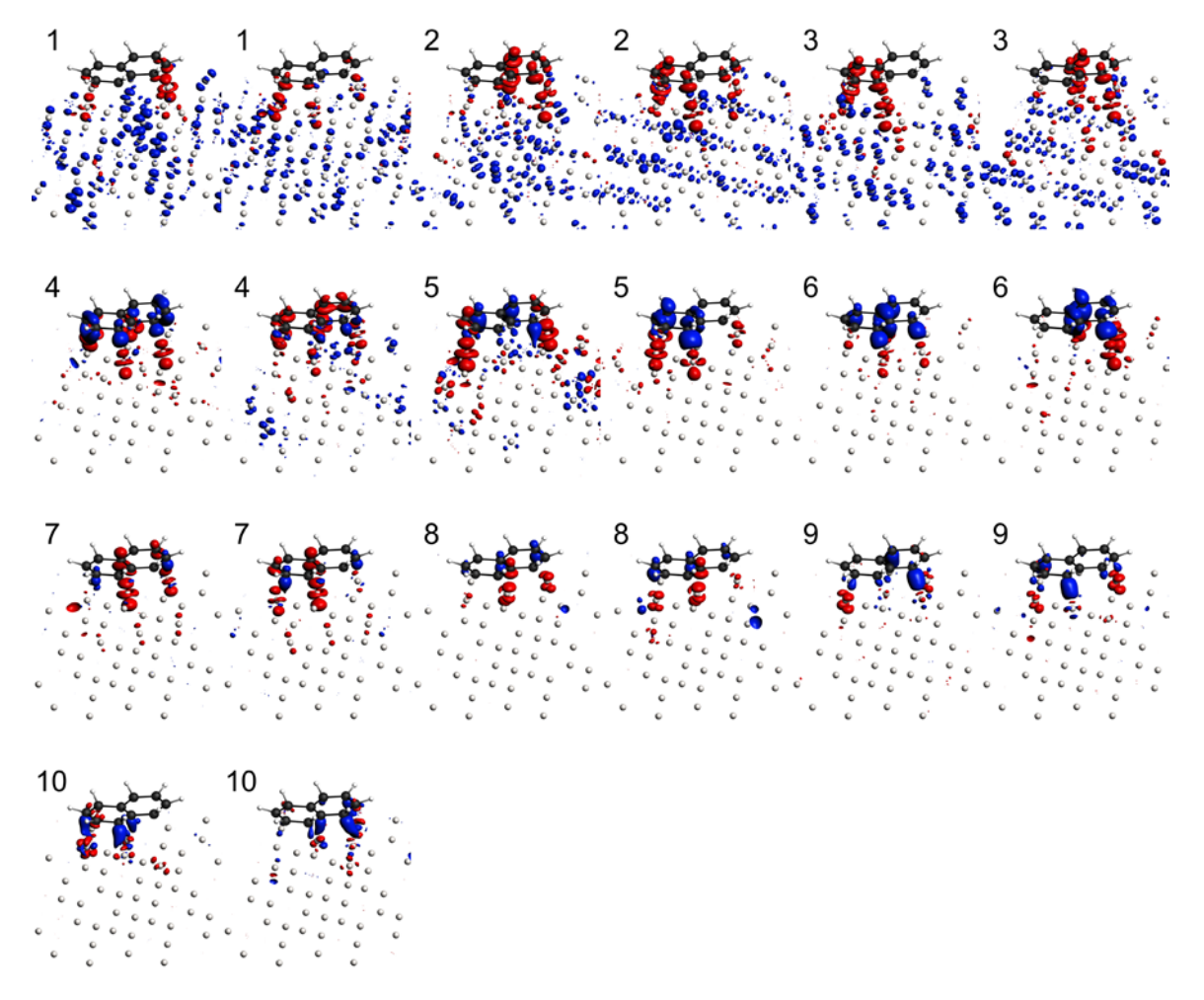


**Figure S7.** NOCV deformation densities  $\Delta \rho_i$  with the largest eigenvalues pEDA plus NOCV analysis for naphthalene on Pt(111). Red, electron depletion; blue, electron accumulation. The number correspond to the numbers in Table S8, left image Spin 1, right image Spin 2. Isosurface values:  $0.003 \text{ e}^{-}/\text{Å}^3$  for 1 to 3,  $0.001 \text{ e}^{-}/\text{Å}^3$  for 4 to 8, and  $0.0005 \text{ e}^{-}/\text{Å}^3$  for 9 and 10. Deformation densities 1 to 3 show electron transfer from the molecule (and sometimes some of the uppermost surface atoms) to the substrate and 4 to 6 show electron transfer from the substrate to the molecule.

**Table S7.** Data for the 10 deformation densities  $\Delta \rho_i$  with the largest eigenvalues in the pEDA plus NOCV analysis and corresponding orbital energy contributions for azulene on Pt(111).  $\Delta E_{\text{orb,rest}}$  indicates the sum of deformation densities than cannot be assigned to a specific interaction.

٨	7/	D٤
$\boldsymbol{\mu}$	1	М І

Spin 1		Spin 2		
NOCV	$\nu_i$ / $e$	$v_i / e$ $\Delta E_{\text{orb,i}} / \text{kJ/mol}$		$\Delta E_{\rm orb,i}$ / kJ/mol
1	±1.000	-139	±1.000	-104
2	$\pm 0.984$	-87	$\pm 0.988$	-70
3	$\pm 0.785$	-43	$\pm 0.780$	-65
4	$\pm 0.697$	-147	$\pm 0.703$	-164
5	$\pm 0.602$	-135	±0.615	-132
6	$\pm 0.514$	-139	±0.532	-157
7	$\pm 0.487$	-158	$\pm 0.479$	-145
8	$\pm 0.454$	-49	$\pm 0.453$	-48
9	$\pm 0.283$	-58	$\pm 0.289$	-55
10	$\pm 0.280$	-56	±0.253	-54
	$\Delta E_{ m orb,rest}$	-481	$\Delta E_{ m orb,rest}$	-480

**Table S8.** Data for the 10 deformation densities  $\Delta \rho_i$  with the largest eigenvalues in the pEDA plus NOCV analysis and corresponding orbital energy contributions for naphthalene on Pt(111).  $\Delta E_{\text{orb,rest}}$  indicates the sum of deformation densities than cannot be assigned to a specific interaction.

## Nt/Pt

Spin 1		Spin 2		
NOCV	$v_i$ / $e$	$v_i / e$ $\Delta E_{\text{orb,}i} / \text{kJ/mol}$		$\Delta E_{\rm orb,i}$ / kJ/mol
1	±1.000	-114	±1.000	-146
2	$\pm 0.988$	-47	$\pm 0.994$	-68
3	$\pm 0.960$	-54	$\pm 0.963$	-50
4	$\pm 0.618$	-154	±0.613	-77
5	$\pm 0.601$	-106	±0.552	-167
6	$\pm 0.551$	-196	±0.551	-173
7	$\pm 0.488$	-71	±0.493	-77
8	$\pm 0.383$	-82	$\pm 0.386$	-80
9	$\pm 0.345$	-88	$\pm 0.348$	-90
10	$\pm 0.310$	-64	±0.312	-67
	$\Delta E_{ m orb,rest}$	-482	$\Delta E_{ m orb,rest}$	-484

#### **XIII.** Technical Details of the DFT Calculations

## Structures and Energies in VASP

The DFT calculations were performed in the Vienna Ab Initio Simulation Package (VASP) Version 5.4.4. <sup>18-21</sup> The PBE functional<sup>22</sup> was used in combination with the third-generation van der Waals dispersion correction by Grimme (DFT-D3)<sup>23-24</sup> and the projector-augmented wave (PAW) ansatz<sup>25-26</sup> for the atomic cores.

The bulk lattice parameter for Pt(111) was optimized using the Birch-Munangham approach yielding a value of 4.072 Å. Using this lattice parameter, a 4-layer slab was constructed.

The plane-wave cutoff energy, the vacuum layer thickness and the k-mesh were determined by convergence series. The resulting values were a cutoff energy of 350 eV and a vacuum layer thickness of 30 Å. The  $\Gamma$ -centered 24×24×1 Monkhorst-Pack k-point mesh of the 1×1 surface cell was adjusted to the supercell size, yielding an 7×7×1 mesh for the (2 $\sqrt{3}$  × 2 $\sqrt{3}$ )R30° supercell.

All structures were optimized using a 0.01 eV/Å force criterion. Only the topmost two surface layers were freely optimized together with the adsorbed molecule, while the bottom two layers were kept frozen at their bulk positions. An extensive search for the best adsorption site was carried out, yielding the on-top-0° site for both molecules, with the azulene molecule slightly rotated. The energies of the free molecules were calculated using a cubic unit cell with an edge length of 30 Å and a Γ-only k-mesh. The frequency calculations were performed in VASP using a finite difference method to calculate the Hessian matrix and the vibrational frequencies. Only displacements for atoms of the molecule and the first surface layer were considered here. The calculation of the thermodynamical corrections yielding the enthalpies was performed as described in the literature.<sup>27</sup>

### pEDA in ADF-BAND

The calculations were performed using ADF-BAND Version 2018.105.<sup>28-29</sup> The same exchange-correlation functional PBE and dispersion correction DFT-D3(BJ)<sup>22-24</sup> as employed in VASP was used here and the ZORA relativistic correction included.<sup>25-26, 30</sup> A Becke grid with good accuracy was employed for the numerical integration.<sup>31</sup> For the atom-centered basis the TZ2P basis set<sup>32-33</sup> with large frozen cores was used.

The structures were taken from the VASP optimizations and not further optimized in ADF-BAND. The calculations of the 4-layer slabs were done with 2D periodic boundary conditions whereas the free molecules were calculated without periodic boundary conditions. The pEDA was performed as implemented in the ADF-BAND package 2018.<sup>28-29, 34</sup> The fragments for the pEDA analysis were chosen to be the surface and the molecule in their singlet ground states. All calculations were performed allowing spin-polarization. For the molecular fragments calculations both with 2D and no periodicity were conducted.

The results of the pEDA were carefully checked for k-space convergence. Table S9 shows the k-space convergence from k-grid  $1\times1$  to  $7\times7$  for both systems. As one can see the convergence is excellent for all contributions.

**Table S9**. k-space convergence for the pEDA calculations, basis set = TZ2P. Shown are the energies in kJ/mol and the deviation to the  $7\times7$  value in percent.

$\Delta E_{\rm int}$	$k$ -grid = $1 \times 1$	$k$ -grid = $3 \times 3$	$k$ -grid = $5 \times 5$	$k$ -grid = $7 \times 7$
Az/Pt	-658 -3.1%	-654 -3.7%	-678 -0.1%	-679
Nt/Pt	-586 -5.5%	-592 -4.4%	-618 -0.3%	-620
$\Delta E_{ m Pauli}$	$k$ -grid = $1 \times 1$	$k$ -grid = $3 \times 3$	$k$ -grid = $5 \times 5$	$k$ -grid = $7 \times 7$
Az/Pt	5979 1.4%	5928 0.5%	5905 0.2%	5896
Nt/Pt	6063 1.5%	6005 0.6%	5986 0.2%	5971
$\Delta E_{ m elstat}$	$k$ -grid = $1 \times 1$	$k$ -grid = $3 \times 3$	$k$ -grid = $5 \times 5$	$k$ -grid = $7 \times 7$
Az/Pt	-3459 0.8%	-3442 0.4%	-3431 0.1%	-3430
Nt/Pt	-3502 0.8%	-3485 0.3%	-3475 0.0%	-3474
$\Delta E_{ m orb}$	$k$ -grid = $1 \times 1$	$k$ -grid = $3 \times 3$	$k\text{-grid} = 5 \times 5$	$k$ -grid = $7 \times 7$
Az/Pt	-2976 1.1%	-2938 -0.2%	-2949 0.2%	-2943
Nt/Pt	-2944 1.0%	-2910 -0.2%	-2926 0.4%	-2915

Table S10 directly compares the pEDA terms of the calculations performed with the  $7\times7$  k-space grid to the values obtained by the NOCV calculation. All energy contributions show a good agreement with deviations of less than 5 % for azulene and less than 9 % for naphthalene. The NOCV analysis, which can only be performed in the  $1\times1$  grid, is therefore expected to give reasonable results and the energetic contributions  $\Delta E_{\rm orb}({\rm surf} \rightarrow {\rm mol})$  and  $\Delta E_{\rm orb}({\rm mol} \rightarrow {\rm surf})$  assigned via the deformation densities are included in Table S6.

**Table S10.** Comparison of the pEDA contributions for  $k=7\times7$  calculations of the regular pEDA analysis and the  $k=1\times1$  ( $\Gamma$ -only) calculations performed for the NOCV extension, all values in kJ/mol.

	Az/Pt		Nt/Pt	
	$k = 7 \times 7$	$k=1\times1$	k=7×7	k=1×1
$\Delta E_{ m int}$	-679	-655	-620	-584
$\Delta E_{\rm int}$ (disp)	-202	-202	-203	-203
$\Delta E_{\rm int}$ (elec)	-476	-453	-417	-381
$\Delta E_{ m Pauli}$	+5896	+5970	+5971	+6055
$\Delta E_{ m elstat}$	-3430	-3457	-3474	-3500
$\Delta E_{ m orb}$	-2943	-2965	-2915	-2936

### **NEXAFS Calculations**

X-ray absorption spectra were calculated using the pseudopotential plane-wave code CASTEP-18.1.<sup>35</sup> For the XPS chemical shifts the delta self-consistent field (DeltaSCF) method of constraining electronic occupations to resemble full core-hole excitations was used. NEXAFS calculations were performed using on-the-fly generated USPPs and the CASTEP module ELNES<sup>36</sup> and the transition-potential approach<sup>37-38</sup>. The structures were taken from the PBE-D3(BJ) calculations mentioned above.

All calculations were performed with the PBE functional, <sup>22</sup> a plane-wave cutoff of 350 eV, and an 8×8×1 Monkhorst Pack k-point grid sampling. We calculated the ground-state electronic structure as well as the density of states (DOS) and the molecular-orbital projected DOS,<sup>39</sup> which reflects the interaction of the free molecular orbitals (MO) with the metal substrate using standard library ultra-soft pseudopotentials (USPPs).<sup>40</sup> MO projections and core-level spectra are processed using a self-written post-processing tool for CASTEP.<sup>39</sup> We calculated XPS chemical shifts using the delta self-consistent field (DeltaSCF) method of constraining electronic occupations to resemble full core-hole excitations. NEXAFS calculations were performed using on-the-fly generated USPPs and the CASTEP module ELNES<sup>36</sup> and the transition-potential approach, <sup>37-38</sup> where the occupation of the initial state orbital (here C 1s) is set to 0.5 and the corresponding Kohn-Sham eigen-energies are taken to reflect the NEXAFS spectrum. Atom-wise projected NEXAFS spectra result from XAS calculations for each individual C 1s center in the corresponding molecule. MO-projected spectra have been generated by multiplying XAS intensities with the absolute overlap matrix element of free azulene and naphthalene frontier molecular orbitals and the band structure of the corresponding adsorbed molecules on the surface. For more details on the computational settings and analysis see Diller et al..41 For more details on the implementation of the molecular orbital projection, see Maurer and Reuter.<sup>39</sup>

#### XIV. References

- 1. Klein, B. P.; van der Heijden, N. J.; Kachel, S. R.; Franke, M.; Krug, C. K.; Greulich, K. K.; Ruppenthal, L.; Müller, P.; Rosenow, P.; Parhizkar, S., et al. Molecular Topology and the Surface Chemical Bond: Alternant Versus Nonalternant Aromatic Systems as Functional Structural Elements. *Phys. Rev. X* **2019**, *9*, 011030.
- 2. Körzdörfer, T.; Kümmel, S. Single-Particle and Quasiparticle Interpretation of Kohn-Sham and Generalized Kohn-Sham Eigenvalues for Hybrid Functionals. *Phys. Rev. B* **2010**, *82*, 155206.
- 3. Kronik, L.; Kümmel, S. Gas-Phase Valence-Electron Photoemission Spectroscopy Using Density Functional Theory. In *First Principles Approaches to Spectroscopic Properties of Complex Materials*, Di Valentin, C.; Botti, S.; Cococcioni, M., Eds. Springer: Berlin, Heidelberg, **2014**; pp 137-191.
- 4. Topping, J. On the Mutual Potential Energy of a Plane Network of Doublets. *Proc. R. Soc. Lond. A* **1927**, *114*, 67-72.
- 5. Albano, E. V. A Model for the Work Function Change Caused by Coadsorption. *Appl. Surf. Sci.* **1983**, *14*, 183-193.
- 6. Eaton, P. E.; Cole, T. W. Cubane. J. Am. Chem. Soc. 1964, 86, 3157-3158.
- 7. Kruszewski, J.; Krygowski, T. M. Definition of Aromaticity Basing on the Harmonic Oscillator Model. *Tetrahedron Lett.* **1972**, *13*, 3839-3842.
- 8. Diederich, F.; Staab, H. A. Benzenoid Versus Annulenoid Aromaticity: Synthesis and Properties of Kekulene. *Angew. Chem. Int. Ed.* **1978,** *17*, 372-374.
- 9. Setiawan, D.; Kraka, E.; Cremer, D. Quantitative Assessment of Aromaticity and Antiaromaticity Utilizing Vibrational Spectroscopy. *J. Org. Chem.* **2016**, *81*, 9669-9686.
- 10. Klein, B. P.; Morbec, J. M.; Franke, M.; Greulich, K. K.; Sachs, M.; Parhizkar, S.; Bocquet, F. C.; Schmid, M.; Hall, S. J.; Maurer, R. J., et al. The Molecule-Metal Bond of Alternant Versus Nonalternant Aromatic Systems on Coinage Metal Surfaces: Naphthalene Versus Azulene on Ag(111) and Cu(111). *J. Phys. Chem. C* 2019.
- 11. Hirshfeld, F. L. Bonded-Atom Fragments for Describing Molecular Charge Densities. *Theor. Chim. Acta* **1977**, *44*, 129-138.
- 12. Bultinck, P.; Van Alsenoy, C.; Ayers, P. W.; Carbó-Dorca, R. Critical Analysis and Extension of the Hirshfeld Atoms in Molecules. *J. Chem. Phys.* **2007**, *126*, 144111.
- 13. Vanpoucke, D. E. P.; Bultinck, P.; Van Driessche, I. Extending Hirshfeld-I to Bulk and Periodic Materials. *J. Comput. Chem.* **2013**, *34*, 405-417.
- 14. Vanpoucke, D. E. P.; Van Driessche, I.; Bultinck, P. Reply to 'Comment on "Extending Hirshfeld-I to Bulk and Periodic Materials". *J. Comput. Chem.* **2013**, *34*, 422-427.
- 15. Bader, R. F. W. *Atoms in Molecules a Quantum Theory*. Oxford University Press: Oxford, **1990**.
- 16. Mitoraj, M. P.; Michalak, A.; Ziegler, T. A Combined Charge and Energy Decomposition Scheme for Bond Analysis. *J. Chem. Theory Comput.* **2009**, *5*, 962-975.
- 17. Pecher, L.; Tonner, R. Deriving Bonding Concepts for Molecules, Surfaces, and Solids with Energy Decomposition Analysis for Extended Systems. *WIREs Comput Mol Sci.* **2019**, *9*, e1401.
- 18. Kresse, G.; Hafner, J. Ab Initio Molecular Dynamics for Liquid Metals. *Phys. Rev. B* **1993**, 47, 558-561.
- 19. Kresse, G.; Hafner, J. Ab Initio Molecular-Dynamics Simulation of the Liquid-Metal-Amorphous-Semiconductor Transition in Germanium. *Phys. Rev. B* **1994**, *49*, 14251-14269.
- 20. Kresse, G.; Furthmüller, J. Efficient Iterative Schemes for Ab Initio Total-Energy Calculations Using a Plane-Wave Basis Set. *Phys. Rev. B* **1996**, *54*, 11169-11186.
- 21. Kresse, G.; Furthmüller, J. Efficiency of Ab-Initio Total Energy Calculations for Metals and Semiconductors Using a Plane-Wave Basis Set. *Comput. Mat. Sci.* **1996**, *6*, 15-50.
- 22. Perdew, J. P.; Burke, K.; Ernzerhof, M. Generalized Gradient Approximation Made Simple. *Phys. Rev. Lett.* **1996,** 77, 3865-3868.

- 23. Grimme, S.; Antony, J.; Ehrlich, S.; Krieg, H. A Consistent and Accurate Ab Initio Parametrization of Density Functional Dispersion Correction (Dft-D) for the 94 Elements H-Pu. *J. Chem. Phys.* **2010**, *132*, 154104.
- 24. Becke, A. D.; Johnson, E. R. Exchange-Hole Dipole Moment and the Dispersion Interaction. *J. Chem. Phys.* **2005**, *122*, 154104.
- 25. Blöchl, P. E. Projector Augmented-Wave Method. Phys. Rev. B 1994, 50, 17953-17979.
- 26. Kresse, G.; Joubert, D. From Ultrasoft Pseudopotentials to the Projector Augmented-Wave Method. *Phys. Rev. B* **1999**, *59*, 1758-1775.
- 27. Pecher, J.; Tonner, R. Precursor States of Organic Adsorbates on Semiconductor Surfaces Are Chemisorbed and Immobile. *Chem. Phys. Chem.* **2017**, *18*, 34-38.
- 28. Band 2018, Scm, Theoretical Chemistry, Vrije Universiteit, Amsterdam, the Netherlands, <a href="http://www.Scm.Com"><u>Http://www.Scm.Com</u></a>.
- 29. te Velde, G.; Baerends, E. J. Precise Density-Functional Method for Periodic Structure. *Phys. Rev. B* **1991**, *44*, 7888.
- 30. Philipsen, P. H. T.; Baerends, E. J. Relativistic Calculations to Assess the Ability of the Generalized Gradient Approximation to Reproduce Trends in Cohesive Properties of Solids. *Phys. Rev. B* **2000**, *61*, 1773-1778.
- 31. Franchini, M.; Philipsen, P. H. T.; Visscher, L. The Becke Fuzzy Cells Integration Scheme in the Amsterdam Density Functional Program Suite. *J. Comput. Chem.* **2013**, *34*, 1819-1827.
- 32. van Lenthe, E.; Baerends, E. J. Optimized Slater-Type Basis Sets for the Elements 1-118. *J. Comput. Chem.* **2003**, *24*, 1142-1156.
- 33. van Lenthe, E.; Baerends, E. J.; Snijders, J. G. Relativistic Regular Two-Component Hamiltonians. *J. Chem. Phys.* **1993**, *99*, 4597-4610.
- 34. Raupach, M.; Tonner, R. A Periodic Energy Decomposition Analysis Method for the Investigation of Chemical Bonding in Extended Systems. *J. Chem. Phys.* **2015**, *142*, 194105.
- 35. Clark, S. J.; Segall, M. D.; Pickard, C. J.; Hasnip, P. J.; Probert, M. I. J.; Refson, K.; Payne, M. C. First Principles Methods Using Castep. *Z. Kristallogr. Cryst. Mater.* **2009**, *220*, 567–570.
- 36. Mizoguchi, T.; Tanaka, I.; Gao, S.-P.; Pickard, C. J. First-Principles Calculation of Spectral Features, Chemical Shift and Absolute Threshold of Elnes and Xanes Using a Plane Wave Pseudopotential Method. *J. Phys.: Condens. Matter* **2009**, *21*, 104204.
- 37. Triguero, L.; Pettersson, L. G. M.; Ågren, H. Calculations of near-Edge X-Ray-Absorption Spectra of Gas-Phase and Chemisorbed Molecules by Means of Density-Functional and Transition-Potential Theory. *Phys. Rev. B* **1998**, *58*, 8097-8110.
- 38. Klues, M.; Hermann, K.; Witte, G. Analysis of the near-Edge X-Ray-Absorption Fine-Structure of Anthracene: A Combined Theoretical and Experimental Study. *J. Chem. Phys.* **2014**, *140*, 014302.
- 39. Maurer, R. J.; Reuter, K. Excited-State Potential-Energy Surfaces of Metal-Adsorbed Organic Molecules from Linear Expansion Δ-Self-Consistent Field Density-Functional Theory (Δscf-Dft). *J. Chem. Phys.* **2013**, *139*, 014708.
- 40. Vanderbilt, D. Soft Self-Consistent Pseudopotentials in a Generalized Eigenvalue Formalism. *Phys. Rev. B* **1990**, *41*, 7892-7895.
- 41. Diller, K.; Maurer, R. J.; Müller, M.; Reuter, K. Interpretation of X-Ray Absorption Spectroscopy in the Presence of Surface Hybridization. *J. Chem. Phys.* **2017**, *146*, 214701.